Sabah, M., Ameri, M. J., Hofmann, H., Ebrahimi, M. (2022): Numerical modeling of injection-induced earthquakes based on fully coupled thermo-poroelastic boundary element method. - Geothermics, 105, 102481.

https://doi.org/10.1016/j.geothermics.2022.102481

Numerical Modeling of Injection-Induced Earthquakes Based on Fully Coupled Thermo-Poroelastic Boundary Element Method

Mohammad Sabah[1], Mohammad Javad Ameri[1], Hannes Hofmann[2], Mohammad Ebrahimi[1]

1-Department of Petroleum Engineering, Amirkabir University of Technology, Tehran, Iran

2- Helmholtz Centre Potsdam GFZ German Research Centre for Geosciences, Potsdam, Germany

Abstract

In recent years, there has been a substantial increase in the induced seismicity associated with geothermal systems. However, understanding and modeling of injection-induced seismicity have still remained as a challenge. This paper presents a two-dimensional fully thermo-hydro-mechanical (THM) coupled boundary element approach to characterize the fault response to forced fluid injection and assess the effect of different injection protocols on seismic risk mitigation as well as permeability enhancement. The laboratory-derived rate-and-state friction law was used to capture the frictional paradigm observed in mature faults produced in granite rocks. All phases of stick-slip cycles, including aseismic slip, propagation of dynamic rupture, and interseismic periods, were simulated. The modeling results showed that the residual values of effective normal stress and static shear stress after a particular event completely dominate the constitutive behavior of fault friction during the next seismic event. The seismic energy analyses indicated that there is a negative correlation between the seismic magnitude and the total injected volume, such that a prolonged monotonic injection eventually results in the steady slip, rather than the seismic slip. Several fluid injection protocols were designed based on a volume-controlled (VC) approach and traffic light systems (TLS) to explore their effectiveness on the seismic risk mitigation and permeability enhancement. The results showed that cyclic injection based on TLS is the most effective approach for irreversible permeability enhancement of faults through promoting slow and steady slips. Our numerical simulations also revealed that fluid extraction (backflow-fixing bottom hole pressure at atmospheric pressure), regardless of the injection style, can considerably reduce the seismicity-related risks by preventing the fast-accelerated fracture slip during the post-injection stage. This study presents novel insights into modeling the rate-and-state governed faults exposed to forced fluid injection, and provides useful approaches for shear stimulation of faults with reduced seismic risks.

Keywords: Induced seismicity, Boundary element method, Monotonic injection, Cyclic injection

1. Introduction

Wastewater injection into deep formations, Hydraulic stimulation of unconventional hydrocarbon reservoirs and enhanced geothermal systems, Co2 sequestration in deep saline aquifers, fluid injection in geothermal reservoirs, and underground natural gas facilities are causal factors behind the anthropogenic earthquakes or the so-called injection-induced seismicity (Brodsky & Lajoie, 2013; Cesca et al., 2014; Deng et al., 2016; Hui, Chen, Chen, et al., 2021; Hui, Chen, Gu, et al., 2021; Shirzaei et al., 2016; Zoback & Gorelick, 2012). In recent years, the dramatic increase in the seismicity rate associated with developing geo-energy systems has raised doubts about the reliability and safety of these renewable energy sources. Forced fluid injection upsets the physical and chemical equilibrium of the pre-existing faults, whereby the local shear stress on the fault may exceed the frictional resistance of the fault surfaces and lead to the injection-induced seismicity (Ji, Zhuang, et al., 2021; Rathnaweera et al., 2020). The decreased level of effective normal stress caused by the injection-induced elevation of pore pressure is considered as an important mechanism behind the occurrence of injection-related seismicity (Wang et al., 2020; Ye & Ghassemi, 2018), and the change in the stress distribution across the pre-existing fractures due to the poroelastic coupling effect (Chang & Segall, 2016a). In addition, the reduced friction coefficient due to fluid lubrication (Dou et al., 2020) and induced changes of temperature and local tectonic stresses may also result in unstable slips (Guglielmi et al., 2015).

Anthropogenic earthquakes mainly manifest as recurrent stick-slip cycles (Brace & Byerlee, 1966; Scholz, 1998), each including three consecutive phases of aseismic slip, seismic rupture propagation, and a interseismic phase (Cueto-Felgueroso et al., 2017). In the first phase, the fault slip may appear as steady-state slips with slip rates below the seismic range. The quasi-static aseismic slips may sufficiently develop along the pre-existing fractures and ultimately lead to nucleation of dynamic instabilities with significantly high slip velocities. Following this, interseismic period begins where quasi-static deformation dominates fault slip behavior. The constitutive behavior of fault friction in each phase of the stick-slip cycle is well characterized by laboratory-derived friction laws. The rate-and-state friction models are the most popular

examples making the friction coefficient dependent on sliding history and slip velocity (Dieterich, 1979; Ruina, 1983; Scholz, 1998). Nevertheless, applying these fully nonlinear constitutive laws in any mathematical model is associated with major computational challenges (Wriggers & Laursen, 2006) that have led many researchers to use more simplified assumptions for fault rheology.

Due to the complexity of interactions between frictional processes and Thermo-Hydro-Mechanical (THM) couplings, developing closed-form solutions for analyzing the induced earthquakes without taking simplifying assumptions is almost impossible (Wu et al., 2021). Despite the fact that laboratory experiments are the basis for characterizing the constitutive behavior of rock friction, they are also associated with some serious limitations in reflecting the whole geomechanical challenges posed by subsurface fluid flow. Numerical modeling has become a major tool to understand the impact of forced-fluid injection on the activation of anthropogenic earthquakes and assess the associated risks. Numerous numerical models have been used to estimate fault reactivation based on different measures, including the tendency to slip, coulomb failure stress, and mobilized friction angle (Andrés et al., 2019; De Simone et al., 2017; Haddad & Eichhubl, 2020; Jeanne et al., 2017; Kettlety et al., 2020; Kim & Hosseini, 2015; Rinaldi & Nespoli, 2017; Vadacca et al., 2021). Recently, thermo-hydro-mechanical models have been developed based on simplified friction models to assess dynamic instabilities that result from the injection/extraction activities (Gan & Lei, 2020; Khademian et al., 2018; Park et al., 2020; Taghipour et al., 2021; Wassing et al., 2021; Yin et al., 2020). Although the proposed models have proved very useful to provide a basic understanding about the role of THM processes on the nucleation of induced earthquakes, they fail to elucidate the whole frictional paradigms observed in the mature faults. Some of the most advanced induced seismicity models introduce the pore pressure and poroelastic stress histories from a separate numerical model to an earthquake simulator (Almakari et al., 2019; Chang & Segall, 2016b; Kroll et al., 2017; Segall & Lu, 2015). But so far, constitutive laws governing the fault frictional behavior are uncoupled to the flow and fault deformations. In other words, in the relevant references, there is one-way coupling between field (Navier and diffusion) equations and rate-and-state friction laws in which pressure and stress tensor are not affected by fault sliding and earthquake nucleation. Over the past

decades, fully-dynamic and quasi-dynamic earthquake simulators combined with rate-and-state friction models have emerged to characterize dynamic ruptures, estimate the magnitude of induced earthquakes, and analyze the role of stress transfer on the triggering mechanisms (Cueto-Felgueroso et al., 2018; Pampillon et al., 2018; Thompson & Meade, 2019; Ziv & Cochard, 2006). Despite the extensive research performed in the field of injection-induced seismicity, especially concerning geo-energy systems, most advanced numerical models still suffer from limitations or simplifying assumptions that make them unable to capture all aspects of induced earthquakes. Moreover, the majority of seismicity-related researches specifically focus on the estimates of fault reactivation and associated risks, and only few attempts have been made to explore the ways to mitigate or avoid potentially damaging earthquakes.

Here, we present a fully coupled THM numerical model combined with the rate-and-state friction model to characterize the fault response to fluid injection and determine how the induced seismicity can contribute to permeability enhancement of a fault existing in a low permeable reservoir without promoting damaging seismic slip events. Our numerical approach is on the basis of displacement discontinuity method (DDM, as a nonlinear model of joint deformation) for a 2-D and thermo-poroelastic domain, which is coupled with finite element method (FEM) to analyze the fluid and heat transport in a fault. Rupture dynamics are resolved in a quasi-dynamic sense, such that some of the fully dynamic effects are captured by adding dynamic radiation terms to the quasi-static equations. This approach prevents instabilities during simulation of dynamic rupture problems and leads to a solution at the end of simulation. A novel solution algorithm is developed to allow the use of a monolithic numerical solution with adaptive time stepping for resolving the fully coupled THM processes and achieving a sufficient numerical resolution during dynamic ruptures. We simulate all stages of each stick-slip cycle, including the aseismic slip, propagation of the rupture and also the interseismic periods. Comprehensive analyses are performed to better understand the role of fully coupled THM on the nucleation of the injection-induced earthquakes and the complexity of the seismic/aseismic slip interactions. Moreover, a part of studies is dedicated to understanding how the fault slip and frictional processes affect the spatiotemporal distribution of dynamic and kinematic parameters around a rate-and-state governed fault.

Although forced-fluid induced seismicity has led to serious doubts about the safety of extracting energy from geothermal systems (Cousse et al., 2021; Knoblauch et al., 2018; Rathnaweera et al., 2020; XinXin et al., 2021), it is capable of enhancing the efficacy of geo-energy systems by means of shear-induced elevation of permeability (Safari & Ghassemi, 2016). In any case, finding a way to prevent the occurrence of large magnitude events and avoid destructive earthquakes is of critical importance. Operational parameters, especially injection rate, are among the parameters that significantly contribute to the nucleation of earthquake, and can be easily controlled by the operator. Recently, cyclic injection has been suggested as an effective solution to decrease or avoid destructive earthquakes (Ji, Yoon, et al., 2021; Ji, Zhuang, et al., 2021; Zang et al., 2019). On the one hand, the majority of studies concerning this matter are limited to the experimental scale and thus the impact of their proposed injection schemes on the nucleation of dynamic instabilities in the field scale remains unclear. On the other hand, a number of previously developed injection regimes are difficult to be experimentally implemented (particularly, the schemes that are based on traffic light systems (TLS)). Hence, we perform a number of numerical experiments to particularly focus on the possibility of seismic risk mitigation by different injection schemes and their contributions to irrecoverable increase in the fault conductivity.

2. Methodology

2.1 Field equations for thermo-poroelastic media

Field equations, which form basis of numerical and mathematical solutions, are derived by combining the governing equations. Such field equations are mainly used, because they result in fewer unknown variables and also more condensed forms of solution systems. In the case of a homogeneous, elastic and isotropic fluid-saturated body, the Navier equation for elasto-static deformations and also diffusion equations for the heat and fluid transport serve as the thermo-poroelastic field equations (Cheng, 2016):

$$G\nabla^2\vec{u} + \left(K + \frac{G}{3}\right)\nabla(\nabla.\vec{u}) - \alpha\nabla P - K\beta_s\nabla T = -F_i \tag{1}$$

$$\frac{\partial P}{\partial t} - KM_{\propto}\nabla^2 P = -\alpha M_{\propto}\frac{\partial e}{\partial t} + \left(\alpha\beta_s + \emptyset\left(\beta_f - \beta_s\right)\right)M_{\propto}\frac{\partial T}{\partial t} - \gamma_f \tag{2}$$

$$\frac{\partial T}{\partial t} - K_T\nabla^2 T = -\gamma_h \tag{3}$$

Here, T and P are temperature and fluid pressure, respectively, u represents the displacement vector, e and F indicate the volumetric strain and body force, respectively. In addition, γ_h and γ_f denote the heat and fluid sources, respectively. The utilized material constants are as the following: K and G represent the bulk and shear moduli, $M_\propto$ and α denote the Biot's modulus and effective stress coefficient, K_T indicates the thermal conductivity, and $\beta_s \; and \; \beta_f$ represent the solid and fluid thermal expansion coefficients, respectively. When employing the boundary element method for a thermo-poroelastic medium, these field equations are transformed into an analytically solvable form by means of a complementary Biot decomposition function, to achieve fundamental solutions. The fundamental solutions, being also known as the influence functions, are singular solutions derived for an infinite elastic medium and serve as the kernels in the boundary integral equations (BIE) (Cheng & Detournay, 1998; Crouch et al., 1983).

2.2 Displacement discontinuity method for quasi-static problems

As mentioned previously, fundamental solutions are derived from singular solutions of thermo-poroelastic field equations without satisfaction of any boundary conditions. Such solutions are associated with a number of BIEs formed on the basis of the reciprocal theorem of Betti and Maxwell (Maxwell, 1864), to solve the elasto-static boundary value problems. Using these equations, which are also called Somigliana Integral Equations (SIE), to model the discontinuities embedded in the poroelastic body is a challenging and complex task. However, SIEs can be changed into an appealing form, specifically suitable for modeling natural fractures, by considering logical assumptions at the boundary. In this approach, that is usually referred to as the displacement discontinuity method (DDM), special distribution densities over space and time are used to mathematically model the fracture surface. With neglecting the chemical effects, these distribution densities mainly include the displacement discontinuity tensor, heat and fluid flux discontinuities, and the fundamental solutions relate their strengths to the kinematic and dynamic parameters at a specific point as follows (Cheng, 2016; Curran & Carvalho, 1987):

$$\sigma_{kl}(x,t) = \int_0^t \int_\Gamma \left[{\sigma_{klij}}^{di}(x-x',t-t') n_j(x') D_{ij}(x',t') + {\sigma_{kl}}^{si}(x-x',t-t') D_f(x',t') + {\sigma_{kl}}^{hi}(x-x',t-t') D_h(x',t') \right] d\Gamma dt' + \sigma_{kl}(x,0) \tag{4}$$

$$P(x,t) = \int_0^t \int_\Gamma \left[{P_{ij}}^{di}(x-x',t-t') n_j(x') D_{ij}(x',t') + P^{si}(x-x',t-t') D_f(x',t') \right. \\ \left. + P^{hi}(x-x',t-t') D_h(x',t') \right] d\Gamma dt' + P(x,0) \quad (5)$$

$$T(x,t) = \int_0^t \int_\Gamma \left[{T_{ij}}^{di}(x-x',t-t') n_j(x') D_{ij}(x',t') + T^{si}(x-x',t-t') D_f(x',t') \right. \\ \left. + T^{hi}(x-x',t-t') D_h(x',t') \right] d\Gamma dt' + T(x,0) \quad (6)$$

Here, σ_{kl} represents the stress tensor, and T and P indicate the temperature and pressure at time t and point x. For the influence functions, ${\sigma_{klij}}^{di}$ is the kl component of induced stress due to the instantaneous displacement discontinuity, D_{ij}, ${\sigma_{kl}}^{si}$ is the kl component of induced stress due to the instantaneous fluid flux discontinuity, D_f, and ${\sigma_{kl}}^{hi}$ is the kl component of induced stress due to the instantaneous heat flux discontinuity, D_h. Physically, the presented fundamental solutions signify the influence of instantaneous impulses at time t' and point x' on stress tensor at distance x and time t. One can define the fundamental solutions for temperature and pressure in a similar manner. The employed distribution densities are as the following: D_{ij} represents the tensor of displacement discontinuity, D_f and D_h denote the fluid and heat flux discontinuities on the surface of fracture, respectively. The initial values of local stresses, temperature, and pore pressure have been shown by $\sigma_{kl}(x,0)$, $T(x,0)$, and $P(x,0)$, respectively. The time marching scheme (Verde & Ghassemi, 2016) is used to evaluate the temporal integration, where temporal integrals are changed into summations, and fundamental solutions associated with instantaneous impulses are transformed into continuous fundamental ones. M elements are utilized for discretization of fracture surface. Displacement discontinuities (D_{ij}) are assumed to be constant across each boundary element, but a linear variation is considered for both the fluid flux (D_f) and the heat flux (D_h) discontinuities. These assumptions not only eliminate the need to significantly increase the number of elements to achieve acceptable accuracy, but also make it possible to easily solve the BIEs simultaneously with the equations discretized by the finite element method (sections 4 and 5). With applying the described mathematical methods, Eqs. 4-6 are written as follows (Ebrahimi et al., 2021):

$$\sigma_{kl}(x,\mathrm{N}\Delta t)=\sum_{m=1}^{M}\int_{\Gamma_m}\begin{pmatrix}{\sigma_{klij}}^{dc}(x-x^m,\Delta t)D_{ij}(x^m,\mathrm{N}\Delta t)\\ +{\sigma_{kl}}^{sc}(x-x^m,\Delta t)N^{(m)}D_f(x^m,\mathrm{N}\Delta t)+{\sigma_{kl}}^{hc}(x-x^m,\Delta t)N^{(m)}D_h(x^m,\mathrm{N}\Delta t)\end{pmatrix}d\Gamma(x^m)$$
$$+\sum_{p=2}^{\mathrm{N}}\sum_{m=1}^{M}\int_{\Gamma_m}\left(\begin{pmatrix}{\sigma_{klij}}^{dc}(x-x^m,p\Delta t)\\ -{\sigma_{klij}}^{dc}(x-x^m,(p-1)\Delta t)\end{pmatrix}D_{ij}(x^m,(\mathrm{N}-p+1)\Delta t)\right.$$
$$+\Big(\big({\sigma_{kl}}^{sc}(x-x^m,p\Delta t)-{\sigma_{kl}}^{sc}(x-x^m,(p-1)\Delta t)\big)\Big)N^{(m)}D_f(x^m,(\mathrm{N}-p+1)\Delta t) \quad (7)$$
$$\left.+\Big({\sigma_{kl}}^{hc}(x-x^m,p\Delta t)-{\sigma_{kl}}^{hc}(x-x^m,(p-1)\Delta t)\Big)N^{(m)}D_h(x^m,(\mathrm{N}-p+1)\Delta t)\right)d\Gamma(x^m)$$
$$+\sigma_{kl}(x,0)$$

$$P(x,\mathrm{N}\Delta t)=\sum_{m=1}^{M}\int_{\Gamma_m}\begin{pmatrix}{P_{ij}}^{dc}(x-x^m,\Delta t)D_{ij}(x^m,N\Delta t)+P^{sc}(x-x^m,\Delta t)N^{(m)}D_f(x^m,N\Delta t)\\ +P^{hc}(x-x^m,\Delta t)N^{(m)}D_h(x^m,N\Delta t)\end{pmatrix}d\Gamma(x^m)$$
$$+\sum_{p=2}^{\mathrm{N}}\sum_{m=1}^{M}\int_{\Gamma_m}\Big(\big({P_{ij}}^{dc}(x-x^m,p\Delta t)-{P_{ij}}^{dc}(x-x^m,(p-1)\Delta t)\big)D_{ij}(x^m,(N-p+1)\Delta t) \quad (8)$$
$$+\big(P^{sc}(x-x^m,p\Delta t)-P^{sc}(x-x^m,(p-1)\Delta t)\big)N^{(m)}D_f(x^m,(N-p+1)\Delta t)$$
$$+\Big(P^{hc}(x-x^m,p\Delta t)-P^{hc}(x-x^m,(p-1)\Delta t)\Big)N^{(m)}D_h(x^m,(N-p+1)\Delta t)\Big)\,d\Gamma(x^m)+\ P(x,0)$$

$$T(x,\mathrm{N}\Delta t)=\sum_{m=1}^{M}\int_{\Gamma_m}\Big(T^{hc}(x-x^m,\Delta t)N^{(m)}D_h(x^m,\mathrm{N}\Delta t)\Big)\,d\Gamma(x^m)$$
$$+\sum_{p=2}^{\mathrm{N}}\sum_{m=1}^{M}\int_{\Gamma_m}\left(\begin{pmatrix}T^{hc}(x-x^m,p\Delta t)\\ -T^{hc}(x-x^m,(p-1)\Delta t)\end{pmatrix}N^{(m)}D_h(x^m,(\mathrm{N}-p+1)\Delta t)\right)d\Gamma(x^m)+T(x,0) \quad (9)$$

Here, $N^{(m)}$ denotes the linear shape function, and N and Δt represent the number and size of time-steps, respectively. Continuous fundamental solutions are indicated by c and boundary element area is denoted by Γ_m. The presented BIEs still need to be evaluated in terms of spatial integrals over boundary elements to achieve a system of algebraic equations. As distribution densities are constant across the boundary elements (constant elements), spatial integrals can be evaluated analytically, and their analytical solutions can be found elsewhere (Tao, 2010; Zhang, 2004). If linear or higher order elements are present, developing analytical solutions is challenging, and numerical techniques such as Gaussian quadrature are used instead to evaluate the spatial integrals. However, numerical integration schemes are computationally expensive

and suffer from less accuracy over elements where x' and x coincide and a higher order of singularity is encountered. In addition, the numerical solution accuracy of BIEs is highly dependent on the level of accuracy provided by the spatial integrals. These two features have led us to follow an analytical approach to solve the spatial integrals related to the influence functions of the heat and fluid flux discontinuities. The analytical derivation of those fundamental solutions can be found in (Ebrahimi et al., 2021).

Discretized stress equations are applied to the center of elements, and BIEs corresponding to the temperature and pore pressure are applied to the element nodes, so as to form a stiffness matrix encapsulating a system of algebraic equations. Therefore, one can rewrite Eqs. 7 to 9 in a vector form, as the following:

$$\sigma_n(t) = A_{nn}D_n(t) + A_{ns}D_s(t) + A_{nf}D_f(t) + A_{nh}D_h(t) + \sigma_{n1} + \sigma_{n0} \quad (10)$$

$$\sigma_s(t) = A_{sn}D_n(t) + A_{ss}D_s(t) + A_{sf}D_f(t) + A_{sh}D_h(t) + \sigma_{s1} + \sigma_{s0} \quad (11)$$

$$P(t) = A_{pn}D_n(t) + A_{ps}D_s(t) + A_{pf}D_f(t) + A_{ph}D_h(t) + P_1 + P_0 \quad (12)$$

$$T(t) = A_{th}D_h(t) + T_1 + T_0 \quad (13)$$

Where, σ_n is the total normal stress, σ_s denotes the shear stress, P is the pressure, and T is the temperature. On the right, D_s and D_n indicate the resulting shear and normal displacements, respectively. P_1, σ_{s1}, σ_{n1}, and T_1 introduce the role of previous time steps in the form of the summation of corresponding terms on the right side of Eqs. 7 to 9, and are directly estimated. The remaining matrixes of coefficients express the fundamental solutions related to the initial time step. Eqs. 10 to 13 result in an equation system consisting of four equations and eight unknowns. Since total number of equations is less than the number of unknown variables, we need four additional equations to get a unique solution. The finite element discretization formulations of the heat and fluid transport in a crack serve as two complementary equations. The other two equations related to the mechanical behavior of crack will be described in the next sections.

2.3 Fluid transport inside the fracture

Here, we model the fault as a one-dimensional (1-D) discontinuity embedded in a two-dimensional (2-D) elastic and porous medium. The cubic law is used to correlate the hydraulic aperture of fault with its permeability. Assuming that temporal changes in fracture opening follow a smooth trend, the flow of an incompressible fluid inside the crack can be considered as darcy flow (Witherspoon et al., 1980; Zimmerman & Bodvarsson, 1996), and so the fluid velocity is:

$$U(x,t) = -\frac{W(x,t)^2}{12\mu}\frac{\partial P(x,t)}{\partial x} \tag{14}$$

Here, W represents the fracture aperture, U, μ and P indicate the fluid velocity, viscosity and pressure inside the fracture and x denotes spatial coordinate. In addition to the cubic law, a mass conservation equation is also needed to reach an equation governing the fluid flow within the fracture. This equation for an incompressible fluid can be expressed as the following:

$$-\frac{\partial q(x,t)}{\partial x} - D_f(x,t) + Q_{inj}\delta\big(x - x_{inj}\big) = \frac{\partial W(x,t)}{\partial t} \tag{15}$$

Here D_f represents the discontinuity of fluid flux in the boundary integral equations (in other words, the fluid source intensity), $\frac{\partial W}{\partial t}$ shows the rate of increase in the volume, and Q_{inj} denotes the rate of injecting fluid at point x_{inj}. The governing equation for fluid transfer within the fault is formulated by substituting Eq. 14 into Eq. 15 as below:

$$\frac{\partial}{\partial x}\left(\frac{W(x,t)^3}{12\mu}\frac{\partial P(x,t)}{\partial x}\right) - D_f(x,t) + Q_{inj}\delta\big(x - x_{inj}\big) - Q_{ext}\delta(x - x_{ext}) = \frac{\partial W(x,t)}{\partial t} \tag{16}$$

The presented governing equation for fluid transport inside the fault is numerically solved by implementing the Galerkin Finite Element Method (GFEM), in which the fracture surface is discretized with the same mesh used for boundary integral equations. Target variables such as fluid pressure are assumed to linearly vary over each element, and their values are approximated

across the elements through linear shape functions and nodal values. The weak formulation of Eq. 16 can be expressed as follows:

$$\sum_{m=1}^{M}[\delta\omega_{i,m} \quad \delta\omega_{j,m}]\left[\left(\int_{\Gamma_m}\left(\left(\frac{\partial N^{(m)}}{\partial x}\right)^T \frac{W^3}{12\mu}\frac{\partial N^{(m)}}{\partial x}\right)d\Gamma\right)\begin{bmatrix}P_{i,m}\\P_{j,m}\end{bmatrix}+\right.$$

$$\left(\int_{\Gamma_m}\left(N^{(m)^T}N^{(m)}\right)d\Gamma\right)\begin{bmatrix}D_{f_{i,m}}\\D_{f_{j,m}}\end{bmatrix}+\left(\int_{\Gamma_m}N^T\left(Q_{ext}\delta(x-x_{ext})-Q_{inj}\delta\big(x-x_{inj}\big)\right)d\Gamma\right)+ \quad (17)$$

$$\left.\left(\int_{\Gamma_m}\left(N^{(m)^T}\right)d\Gamma\right)\frac{\partial W}{\partial t}\right]=0$$

One can rewrite the above relationship and use the fundamental lemma of the calculus of variation, to obtain a condensed form of Eq. 17 as the following:

$$A_1P^{n+1}+A_2{D_f}^{n+1}=A_3\frac{W^{n+1}-W^n}{\Delta t}+Q_{inj}-Q_{ext} \quad (18)$$

Where,

$$A_2=\underset{m=1}{\overset{M}{Assemble}}\int_{\Gamma_m}\left(\left(\frac{\partial N^{(m)}}{\partial x}\right)^T\frac{{W^{(m)}}^3}{12\mu}\frac{\partial N^{(m)}}{\partial x}\right)d\Gamma \quad (19)$$

$$A_2=\underset{m=1}{\overset{M}{Assemble}}\left(\int_{\Gamma_m}\left(N^{(m)^T}N^{(m)}\right)d\Gamma\right) \quad (20)$$

$$A_3=\underset{m=1}{\overset{M}{Assemble}}\left(\int_{\Gamma_m}\left(N^{(m)^T}\right)d\Gamma\right) \quad (21)$$

$$N^{(m)}=\begin{bmatrix}\dfrac{x-x_j}{x_j-x_i} & \dfrac{x-x_i}{x_j-x_i}\end{bmatrix} \quad (22)$$

Where n shows the time step, and $Assemble$ represents the process of assembly. Eq. 18 results in a number of algebraic equations of linear type, the number of which being equal to the number of unknown variables. But, achieving a unique pressure distribution within the fracture requires one initial condition and two boundary conditions. The initial distribution of pressure within the fracture is considered as the initial condition for numerical evaluation of Eq. 18. There is a Newman type boundary condition, assuming that the fluid flux normal to the crack tips is zero (Yew, 1997):

$$-\frac{W^3}{12\mu}\left(\frac{\partial P}{\partial n}\right)_{x_e}=0 \quad (23)$$

Here n is a vector outward and normal to the fracture edge and x_e denotes the edges of fracture. The above condition shows that there is no leak-off from fracture into the rock matrix only at the normal direction to the fracture tips, which is applied implicitly when deriving the weak formulation of Eq. 16 and thus, it is not directly used to solve Eq. 18. For boundary value problems concerning injection into a fracture, it is not applicable to set a pressure level on any node so as to define an essential boundary condition. Hence, if Eq. 18 is solved by applying only one Newman type boundary condition, the resulting solution in addition to any arbitrary fixed value can also satisfy it. For a particular problem, this fixed value can be determined by adding a constant pressure (P_c) to Eq. 18:

$$A_1[P^{n+1} + P_c] + A_2 {D_f}^{n+1} = A_3 \frac{W^{n+1} - W^n}{\Delta t} + Q_{inj} - Q_{ext} \tag{24}$$

The above equation can be rewritten as follows:

$$A_1 P^{n+1} + A_2 {D_f}^{n+1} + A_c P_c = A_3 \frac{W^{n+1} - W^n}{\Delta t} + Q_{inj} - Q_{ext} \tag{25}$$

Where A_c represents an $(M \times 1)$ vector and P_c is a constant level that requires updating at each time step. Due to the increase in the number of unknown functions, a compatibility condition is required to reach the unique solution. Global mass balance equation can satisfy the required condition (Yew, 1997):

$$\int_{\partial\Gamma_i} Q_{inj} ds - \int_{\partial\Gamma_e} Q_{ext} ds - \int_{\Gamma} D_f dx = \int_{\Gamma} \frac{\partial W(x,t)}{\partial t} d\Gamma \tag{26}$$

Here $\partial\Gamma_e$ and $\partial\Gamma_i$ indicate the extraction and injection well areas, respectively. The global mass conservation formulation can be discretized using GFEM as the following:

$$A_e {D_n}^{n+1} + \Delta t A_e T_R D_f = Q_{inj} \Delta t + A_e (W^n - W_0) \tag{27}$$

Here ${D_n}^{n+1}$ represents the fracture aperture (i.e. discontinuity of normal displacement) induced at time step $n+1$, W_0 and W^n denote the fracture apertures at time zero and time step n, respectively, A_e is a $(1 \times M)$ vector of element area, and T_R represents the transformation matrix that is based on nodal values and is used to specify pressure levels at element centroids.

2.4 Heat transport inside the fracture

The equation which governs the heat transport within the crack can be derived by combining the Fourier's laws and energy conservation. In the case of continuous fluid injection, heat accumulation is insignificant in comparison to the diffusion and advection heat transport owing to the fluid movement. Neglecting the heat storage simplifies the governing equation by dropping the term including the time derivative (Diersch, 2013), as the following:

$$\rho_f C_f U(x,t) W(x,t) \frac{\partial T}{\partial x} - K_f W(x,t) \frac{\partial^2 T}{\partial x^2} + D_h(x,t) = 0 \tag{28}$$

Where ρ_f is fluid density, C_f is specific heat capacity, and K_f is heat conductivity. Rest of the parameters have been described in previous sections. Eq. 28, which is a second-order and hyperbolic Partial Differential Equation (PDE), is also called the advection-diffusion equation. The GFEM approach produces unstable and oscillatory solutions for such equations, especially when highly nonlinear variations are present. The Streamline Upwind Petrov Galerkin (SUPG) technique (Brooks & Hughes, 1982), which modifies weight functions depending on the advection intensity and flow direction, can be used instead. This approach involves adjusting weight functions through adding streamline upwind effect ($N^{(m)'}$) to the corresponding shape functions, thereby leading to the discontinuity of weight functions over the boundaries of element. With using the SUPG numerical technique, Eq. (28) can be discretized as follows:

$$\begin{aligned}\sum_{m=1}^{M} [\delta\omega_{i,m} \quad \delta\omega_{j,m}] \Bigg[& \rho_f C_f \left(\int_{\Gamma_m} \left(N^{(m)} + N^{(m)'} \right)^T U^{(m)} W^{(m)} \frac{\partial N^{(m)}}{\partial x} d\Gamma \right) \begin{bmatrix} T_{i,m} \\ T_{j,m} \end{bmatrix} \\ & + K_f \left(\int_{\Gamma_m} \left(\frac{\partial N^{(m)}}{\partial x} \right)^T W^{(m)} \frac{\partial N^{(m)}}{\partial x} d\Gamma \right) \begin{bmatrix} T_{i,m} \\ T_{j,m} \end{bmatrix} \\ & + \left(\int_{\Gamma_m} \left(N^{(m)} + N^{(m)'} \right)^T N^{(m)} d\Gamma \right) \begin{bmatrix} D_{h\,i,m} \\ D_{h\,j,m} \end{bmatrix} \Bigg] = 0 \end{aligned} \tag{29}$$

The following equations give the condensed form of the Eq. 29 via implementing the fundamental lemma of the calculus of variations:

$$A_4 T^{N\Delta t} + A_5 {D_h}^{N\Delta t} = 0 \tag{30}$$

Where,

$$A_4 = \underset{m=1}{\overset{M}{Assemble}} \left(\begin{array}{c} \rho_f C_f \left(\int_{\Gamma_m} \left(N^{(m)} + N^{(m)'} \right)^T U^{(m)} W^{(m)} \dfrac{\partial N^{(m)}}{\partial x} d\Gamma \right) \\ + K_f \left(\int_{\Gamma_m} \left(\dfrac{\partial N^{(m)}}{\partial x} \right)^T W^{(m)} \dfrac{\partial N^{(m)}}{\partial x} d\Gamma \right) \end{array} \right) \tag{31}$$

$$A_5 = \underset{m=1}{\overset{M}{Assemble}} \int_{\Gamma_m} \left(N^{(m)} + N^{(m)'} \right)^T N^{(m)} d\Gamma \tag{32}$$

2.5 Shear and Normal Deformations

It is assumed that the fracture is hydraulically open and mechanically closed when the fracture surface is subjected to non-zero levels of effective normal stress. In this case, the relationship between the total normal stress and the joint normal deformation can be described based on the fracture normal stiffness, K_n, as follows (Ebrahimi et al., 2021):

$$\sigma_n(t) - \sigma_{n0} = K_n(t) D_n(t) + K_{n1} + (P_0 - P(t)) \tag{33}$$

Where σ_n and σ_{n0} are total normal and initial stresses, respectively. K_{n1} refers to the effect of previous time steps and can be defined as below:

$${K_{n1}}^{(m)} = \sum_{p=1}^{\mathrm{N}} \big(K_n(x_m, (p-1)\Delta t) - K_n(x_m, p\Delta t) \big) D_n(x_m, (p-1)\Delta t) \tag{34}$$

Here m represents the number of a certain element on the boundary. Normal stiffness is highly sensitive to variations in the joint normal closure and magnitude of effective normal stress on the crack surface. In the present study, we have used the modified Barton-Bandis model, to update the value of $K_n(t)$ as the following (Bandis et al., 1983; Barton et al., 1985):

$$K_n(t) = \frac{K_{ni}}{\left(1 - {D_n(t)}/{D_{nmax}}\right)^2} \tag{35}$$

This model is based on the dependency of the normal stiffness on the normal closure of fracture and also some constants that have been experimentally obtained. In the above equation, K_{ni} is the initial normal stiffness under the initial effective normal stress, and D_{nmax} is the maximum

normal closure. These constants can be easily determined through laboratory experiments. Eq. 35 shows that a decrease in the normal opening, associated with an increase in the normal effective stress, enhances the normal stiffness, which tends to infinity when the normal opening reaches the maximum normal closure. This implies that under high normal effective loads, variation in the fracture aperture is mainly dominated by the maximum normal closure, rather than the normal stiffness and stress. When the fluid is being injected, the value of normal stiffness is reduced with the reduction in the effective normal stress and when this parameter reaches zero (where the fracture is open hydraulically and mechanically), the stress-closure relationship can no longer be described by Eq. 35. For shear deformation of rock joints, the magnitude of the shear stress applied on the fault surface and the amount of increase in the shear displacement are linearly related to each other, as below:

$$\sigma_s(t) - \sigma_{s0} = K_s D_s \tag{36}$$

Where, σ_s and σ_{s0} are the total and initial shear stresses, and K_s and D_s are the shear stiffness and displacement, respectively. We use Eq. 36 as constitutive equation for modeling the behavior of fracture in the shear direction when the magnitude of shear stress is smaller than the shear strength of the fault. As the shear stress exceeds the fault shear strength, the fault shear deformation is no longer in the linear elastic range, and special constitutive friction laws should be implemented to model the fault seismic response.

2.6 Rate-and-State Friction Laws

Conventional notions of dynamic and static friction are extended by rate-and-state friction laws through integrating the friction coefficient dependence on the sliding history and slip velocity (Baumberger & Caroli, 2006; Dieterich, 1979; Rice, 1983; Ruina, 1983). These models, which are derived based on experimental studies, can accurately describe the friction-related behavior of sliding interfaces in response to the variations in slip rate (Marone, 1998). Based on the rate-and-state friction models, for frictional interfaces sliding with slip rate V, the friction coefficient can be formulated as follows (Ruina, 1983):

$$\mu = \mu^* + aln\left(\frac{V}{V^*}\right) + bln\left(\frac{\theta}{\theta^*}\right) \tag{37}$$

Here μ^* indicates the coefficient of steady-state friction at the reference slip velocity that is denoted by V^*, while b and a represent the parameters of evolution friction and direct effect,

respectively. θ refers to the state variable and incorporates the sliding history. $\theta^* = \frac{D_c}{V^*}$ denotes the value of state variable under steady-state conditions at V^*. D_c represents the characteristic distance. It is the length scale that is needed for the evolution of the frictional coefficient after the occurrence of a perturbation in the system (Dieterich, 1978; Marone, 1998). There are also various rate-and-state friction models categorized based on different definitions proposed for evolution of the state variable. The advantages and limitations of these proposed models have been thoroughly examined through analytical and numerical studies (Mitsui & Hirahara, 2009; Putelat et al., 2011; Van den Ende et al., 2018) and model-experimental comparisons (Bhattacharya et al., 2017). In this study, the classical version of aging law is used to model the evolution of the state variable:

$$\frac{d\theta}{dt} = 1 - \frac{V\theta}{D_c} \tag{38}$$

There are other alternative approaches to model the variation of the state variable, for example different composite laws (Kato & Tullis, 2001) and slip law (Ruina, 1983), but finding a formulation that is best able to capture the experimental results is still the subject of research (Bhattacharya et al., 2015; Bhattacharya et al., 2017; Shreedharan et al., 2019). The numerical approach proposed in this study can be readily applied to different classical rate-and-state laws and modified models that incorporate variability in the shear and effective normal stresses (Linker & Dieterich, 1992; Nagata et al., 2012).

2.7 Criteria for Spatial Discretization

Accurate model response may not be captured by the existing numerical solution algorithms, if length of a particular boundary element, Δx, is not small enough. When the shear stress acting on the frictional interfaces exceeds the frictional resistance, steady slip occurs and develops along the fault prior to transforming into a fully seismic slip. One of the prerequisites for the onset of a dynamic instability is that the length of the steadily sliding interface exceeds the earthquake nucleation size h^* (Lapusta et al., 2000). Earthquake nucleation size can be estimated from two theoretical formulations (Rice & Ruina, 1983; Rubin & Ampuero, 2005), which are derived for two-dimensional problems:

$$h^*_{RR} = \frac{\pi}{4}\frac{G^* D_c}{(b-a)\sigma} \tag{39}$$

$$h^*_{RA} = \frac{2}{\pi}\frac{G^* D_c b}{(b-a)^2\sigma} \tag{40}$$

where $G^* = \frac{G}{(1-\vartheta)}$. The estimate h^*_{RR} has been derived based on analyzing the stability of steady slips on the velocity-weakening region of faults (Rice & Ruina, 1983). h^*_{RA} has been proposed based on the energy balance concept for cracks extending in a quasi-static manner (Rubin & Ampuero, 2005). This estimate of nucleation size is only applicable for the parameter regime $a/b > 0.5$. Several researchers (Ben-Zion & Rice, 1997; Lapusta et al., 2000; Rice, 1993) suggest that h^* is a critical length scale governing the interseismic processes, in particular, the earthquake nucleation phase. Hence, h^* should be considered in the modeling process to reach an appropriate resolution for simulation of earthquake phases associated with quasi-static sliding. However, one should employ an additional resolution criterion for controlling numerical resolution when the rupture is propagating. In previous researches, a parameter called the cohesive zone size, Λ, has been introduced, which indicates a spatial length scale needed to reduction of shear stress at the propagating front of rupture from its maximum level to a residual level (Day et al., 2005). So, $\Lambda/\Delta x$ is a parameter that is crucial for resolving dynamic ruptures. Λ can be formulated as follows:

$$\Lambda = 9\pi\frac{G^* D_c}{b\sigma} \tag{41}$$

Day et al., (2005) suggested a $\Lambda/\Delta x$ value in the range of 3 to 5 is for achieving resolution-independent results and resolving the dynamic ruptures. According to Lapusta & Liu, (2009) studies, the cohesive zone size is generally the restrictive condition for spatial discretization of the fault surface. But, with respect to the state and rate parameters, the size of cells should be sufficiently small, so as to meet the requirements of the most restrictive resolution criteria.

2.8 Quasi-dynamic Earthquake Simulation

Quasi-dynamic earthquake simulation is an efficient technique for examining the injection-induced earthquake sequences without requiring the computational resources necessary for fully dynamic models (Cueto-Felgueroso et al., 2017; Liu & Rice, 2005; Thompson & Meade, 2019). Implementing the quasi-dynamic modeling instead of a fully dynamic approach simplifies the mathematical formulation and significantly reduces the computationally expensive numerical processes. In the quasi-dynamic modeling approach, the wave-induced stress transfers are neglected and hence, any increase in the shear displacement results in the instantaneous alteration of static stress across the fault. However, the radiation damping term, ηV, appearing in the fully dynamic formulation, is also retained in the quasi-dynamic approach, making it possible to capture most of the fully dynamic effects while maintaining the solution during dynamic instabilities. For the generalized quasi-dynamic formulation, the shear traction acting on the fault surface during slippage can be expressed as follows:

$$\tau_f = \tau_{static} - \eta V$$
$$\eta = \frac{G}{2c_s\beta_s} \tag{42}$$

Where c_s is the shear wave speed, V is the slip velocity, G represents the shear modulus, τ_f is the frictional strength of fault, and τ_{static} denotes the shear traction on the fault surface calculated from quasi-static equations. β_s is a constant which is used to intensify the ignored wave effects. In this study, β_s is set to 3 based on numerical experiments conducted by Lapusta & Liu, (2009). One can use the following formulation to calculate the frictional resistance magnitude for a fault or natural fracture:

$$\tau_f = \mu\sigma_n{}' \tag{43}$$

In order to model earthquakes in the quasi-dynamic sense, one should implement the fully-coupled model including the boundary integral equations (Eqs. 10 to 13), together with evolution of μ and θ (Eqs. 37 to 38), and the fault strength model (Eqs. 42&43).

2.9 Computational Procedure

The fault response to the pore pressure and stress perturbation appears as short bursts of rapid slip followed by long-term quasi-static deformation. Simulation of such responses requires utilization of relatively long time steps (for example, a part of a day) to analyze the quasi-static type deformation within interseismic periods. On the other hand, much smaller time steps (less than a second) are needed for dynamic rupture simulation. However, numerical approaches based on the thermo-poroelastic displacement discontinuity method are not compatible with adaptive time stepping, which poses major challenges for simulating earthquake sequences. To address this, we employed the elastic DD method (Crouch et al., 1983) as a complementary numerical approach that makes it possible to use adaptive time stepping as soon as the fault is activated, without changing the initial time step size considered for the thermo-poroelastic DD. This means that there will be two sets of time stepping, a constant time stepping for the thermo-poroelastic DD and an adaptive time stepping for the elastic one. At the beginning, the first prediction of shear displacement is made at time $t + \Delta t$, assuming that the shear displacement at time $t + \Delta t$ is equal to that in the previous time step. Afterwards, the thermo-poroelastic BIEs (Eqs. 10 to 13), fluid transport equation (Eq. 18, 27), heat transport equation (Eq. 30), and complementary equations (Eqs. 33&36) are solved simultaneously in a fully coupled manner at time $t + \Delta t$ as follows:

$$\begin{bmatrix} A_1 & 0 & 0 & 0 & A_2 & 0 & A_c \\ -T_R & 0 & -A_{nn} & -A_{ns} & -A_{nf} & -A_{nh} & -T_R I_0 \\ 0 & 0 & -A_{sn} & -A_{ss} & -A_{sf} & -A_{sh} & 0 \\ I & 0 & -A_{pn} & -A_{pn} & -A_{pn} & -A_{ph} & I_0 \\ 0 & 0 & A_e & 0 & A_e T_R \Delta t & 0 & 0 \\ 0 & A_4 & 0 & 0 & 0 & A_5 & 0 \\ 0 & I & 0 & 0 & 0 & -A_{th} & 0 \end{bmatrix} \times \begin{bmatrix} P^{n+1} \\ T^{n+1} \\ {D_n}^{n+1} \\ {\sigma_s}^{n+1} \\ {D_f}^{n+1} \\ {D_h}^{n+1} \\ {P_c}^{n+1} \end{bmatrix} = \begin{bmatrix} A_3 \dfrac{W^{n+1} - W^n}{\Delta t} + Q_{inj} - Q_{ext} \\ \sigma_{n1} - P_0 - K_{n1} \\ \sigma_{s1} + \sigma_{s0} + A_{ss} D_s(t) \\ P_1 + P_0 \\ \Delta t\left(Q_{inj} - Q_{ext}\right) + A_e(W^n - W_0) \\ 0 \\ T_1 + T_0 \end{bmatrix} \quad (44)$$

Gaussian elimination method is used to solve the above algebraic equations, yielding the distribution densities (D_f, D_n, D_h), shear stress, temperature and pressure changes along the fault at time $t + \Delta t$. Then, the effective normal stress applied on the fault surface is calculated, and it is assumed that the value of this kinematic parameter on each of the boundary elements varies linearly over the time step as follows:

$$\sigma_n{}' = \begin{bmatrix} \frac{t' - (t + \Delta t)}{\Delta t} & \frac{t' - t}{\Delta t} \end{bmatrix} \begin{bmatrix} \sigma_n{}'(t + \Delta t) \\ \sigma_n{}'(t) \end{bmatrix} \quad (45)$$

$$t' = t + \Delta t'$$

This assumption allows calculating the effective normal stress on boundary elements at any arbitrary time t' in the time interval $[t, t + \Delta t]$. $\Delta t'$ refers to a variable time step size, implemented to capture the evolution of the dynamic ruptures if dynamic instability occurs in the prescribed time interval. Afterward, the solution procedure is switched to the elastic DD method to apply the adaptive time stepping if necessary. In this study, we use the adaptive time stepping scheme proposed by Lapusta & Liu, (2009) for two-dimensional problems. The variable time step $\Delta t'$ is determined as follows:

$$\Delta t' = max\{\Delta t_{min}, \Delta t_{evol}\} \quad (46)$$

Where Δt_{min} is the minimum time step required to reach a good resolution during dynamic instabilities, and Δt_{evol} is a variable time step depending on the maximum slip velocity. The minimum time step is calculated based on the spatial cell size and shear wave velocity as follows:

$$\Delta t_{min} = \gamma \Delta x / c_s \quad (47)$$

Where γ is a constant. and γ is set to $1/3$, according to previous reports (Lapusta & Liu, 2009; Lapusta et al., 2000). The variable time step Δt_{evol} is inversely related to slip velocity and directly related to the characteristic length:

$$\Delta t_{evol} = \xi D_c / V \quad (48)$$

Here ξ is a function that depends on frictional variables and is obtained through analysis of linear stability (Lapusta et al., 2000). In the numerical scheme presented in this study, we use $\xi = 0.01$. After setting the time step size, the second order Runge-Kutta (midpoint) procedure is used to predict the values of slip, state variable and slip velocity at the next time step, $\Delta t'$. The first predictions corresponding to the shear displacement and state variable are made at the time $t + \Delta t'/2$ for each boundary element, assuming that slip rates are constant and the same as those

obtained in the previous time step. Therefore, shear displacement and state variable can be obtained as follows:

$$D_s(t+\Delta t'/2) = D_s(t) + V\,(t)\Delta t'/2$$
$$\theta(t+\Delta t'/2) = \Delta t/2\left(1-\frac{\theta(t)V\,(t)}{D_c}\right)+\theta(t) \quad (49)$$

Following this, the quasi-static shear stress, $\sigma_s(t+\Delta t'/2)$, is calculated based on $D_s(t+\Delta t'/2)$ and the initial value of shear stress, σ_{s0}, using the elastic DD method. Then, by combining the generalized quasi-dynamic equation (Eq. 42) with the rate-and-state friction law (Eq. 37), the following equation is obtained to approximate the value of slip velocity at time $t+\Delta t'/2$:

$$\left[\mu^* + aln\left(\frac{V}{V^*}\right)+bln\left(\frac{\theta(t+\Delta t'/2)}{\theta^*}\right)\right]\sigma_n{}' = \sigma_s(t+\Delta t'/2)-\frac{G}{2\beta_s c_s}V \quad (50)$$

Eq. (50) is solved for $\mathrm{V}(t+\frac{\Delta t'}{2})$ using the Newton-Raphson search. Then, the obtained slip velocity is used to approximate the values of shear displacement and state variable at time $t+\Delta t'$ as follows:

$$D_s(t+\Delta t') = D_s(t)+\Delta t\mathrm{V}(t+\Delta t'/2)$$
$$\theta(t+\Delta t') = \Delta t\left(1-\frac{\theta(t)\mathrm{V}(t+\Delta t'/2)}{D_c}\right)+\theta(t) \quad (50)$$

State variable $\theta(t+\Delta t')$ and shear stress $\sigma_s(t+\Delta t')$ are fed into Eq. 49 to calculate the second prediction of slip velocity $\mathrm{V}(t+\Delta t')$. All these processes are repeated for the next time step as long as the sum of time steps is equal to Δt, the size of time interval $[t, t+\Delta t]$. The last time step would yield the shear displacement at time $t+\Delta t$, which can be used as the second prediction of the value of D_s for the thermo-poroelastic solution process. The fault normal opening, pressure distribution and effective normal stresses on the fault surface are corrected based on the new value of $D_s(t+\Delta t)$ with solving Eq. 44. Finally, the corrected values of normal displacement and effective normal stress are used in the elastic solution process to apply the adaptive time stepping. This iteration loop continues between the elastic DD and the thermo-poroelastic one until stratifying a convergence criterion. All of above procedures has been shown as a flow chart in Fig. 1.

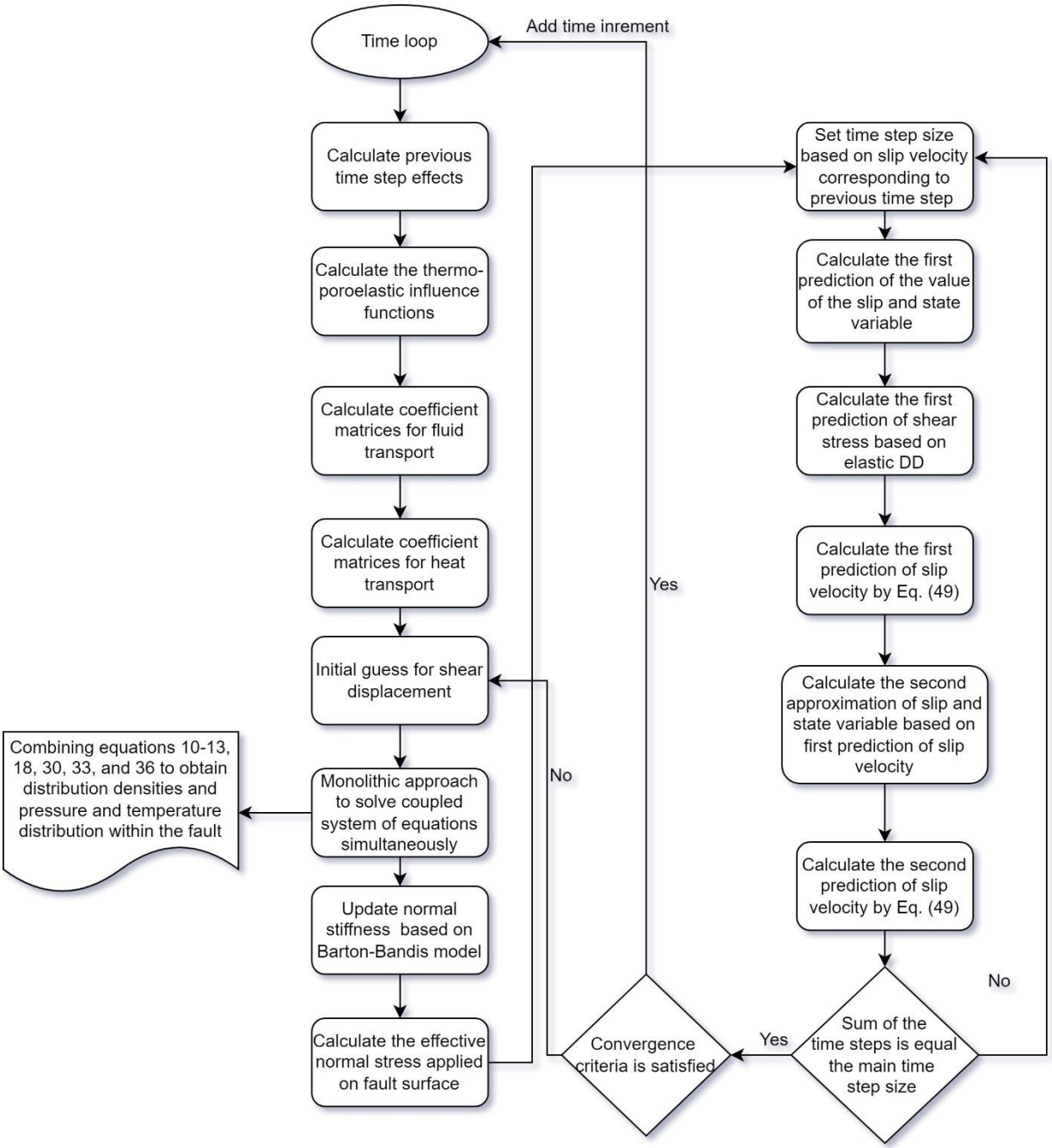

Fig. 1. Flow chart of numerical solution procedure to simulate the injection-induced seismicity

3. Model validation

Many semi-analytical and analytical techniques have been developed to address the crack-related coupled phenomena. On the one hand, simplifying assumptions form the basis of these solutions, and therefore they fail to fully analyze the complex thermo-hydro-mechanical coupled issues. On the other hand, analytical solutions can serve as reliable standards for numerical techniques and can be utilized to validate the developed models. In this study, two closed-form solutions, developed for assessing temperature and fracture aperture variation under different boundary conditions, are implemented to test the reliability of the proposed fully coupled numerical model.

Firstly, the analytical solution established for the distribution of fluid temperature inside a fracture is used to verify the feasibility of the proposed numerical model in terms of heat transport. Cheng et al., (2001) have proposed an analytical solution for spatiotemporal temperature distribution of a fluid within a single 2-D fracture along the x-axis:

$$T_f = T_{ro} + (T_{inj} - T_{ro}) erf\left(\frac{K_r x}{d_{fr} U_{inj} C_f} . \sqrt{\frac{\rho_r C_r U_{inj}}{K_r \left(U_{inj} t - x\right)}}\right) \quad (51)$$

Here, U_{inj} denotes the fluid velocity inside the fracture, T_{inj} and T_{ro} are initial rock and injected fluid temperature, respectively, and d_{fr} shows the fracture aperture. This analytical solution is developed based on some simplifying assumptions as the following: the rock matrix is unbounded in the y-direction, fracture aperture is a constant value, and conduction and advection dominate the heat transport within the rock matrix and fracture, respectively. The model parameters along with the geometric model for heat transfer within the single fracture are shown in Fig. 2. 50 equal-length 1-D elements are used to discretize the fracture surface. The fluid is injected from the fracture tip at the right side, assuming that fracture walls are impermeable (No leak-off). Fig.2 indicates a comparison of numerical and analytical solutions corresponding to temperature distribution within the fracture due to fluid injection. Fig. 3(a) shows temperature changes within the fracture at different times (i.e. 20, 90, 180, 270, and 365 days), while Fig. 3(b) illustrates temperature changes over 365 days at four different positions (100, 400, 600, and 1000 m) along the fracture. It is noticeable that the numerical results are in good agreement with the analytical

solution, which indicates the reliability of the proposed numerical solution algorithm for heat transport.

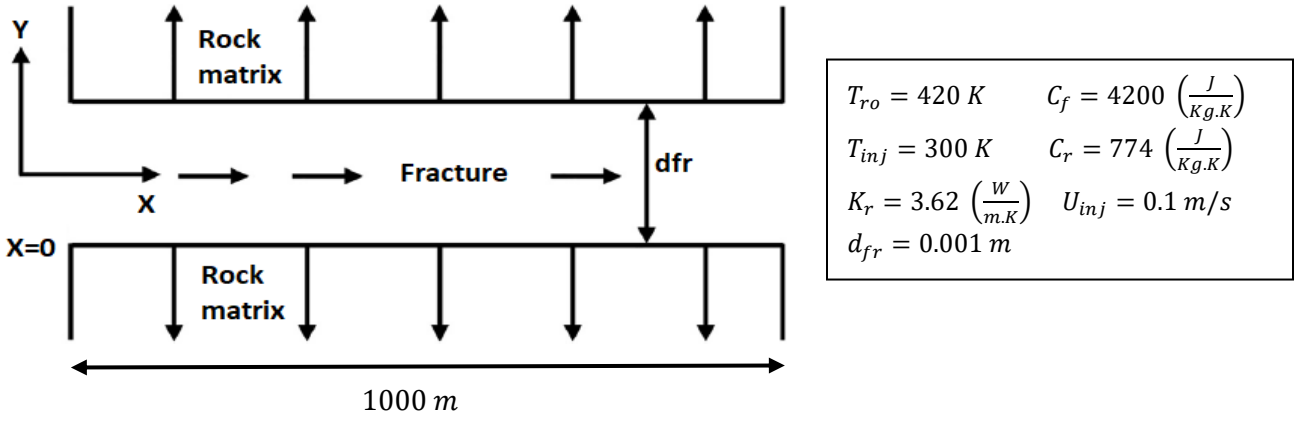

Figure 2. Schematic conceptual model of heat transfer in a single fracture and corresponding model parameters.

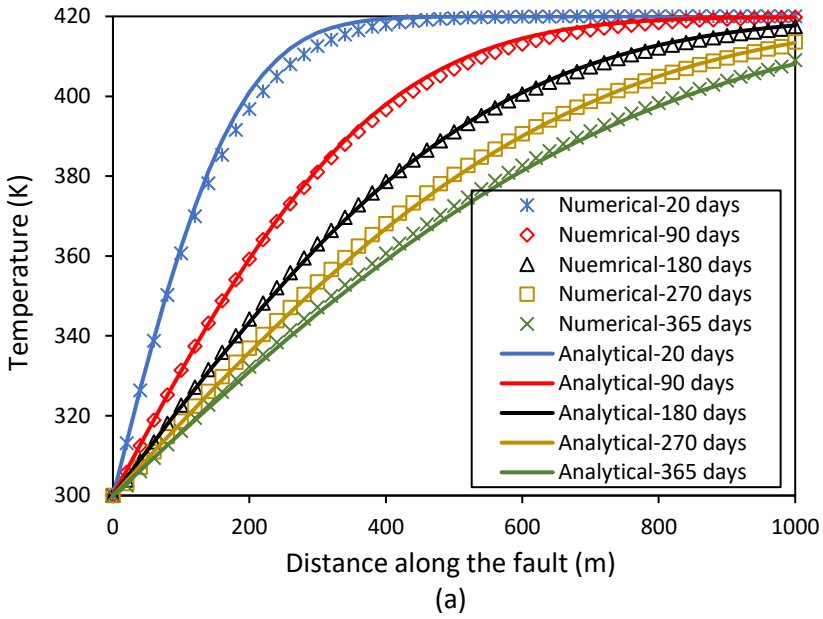

(a)

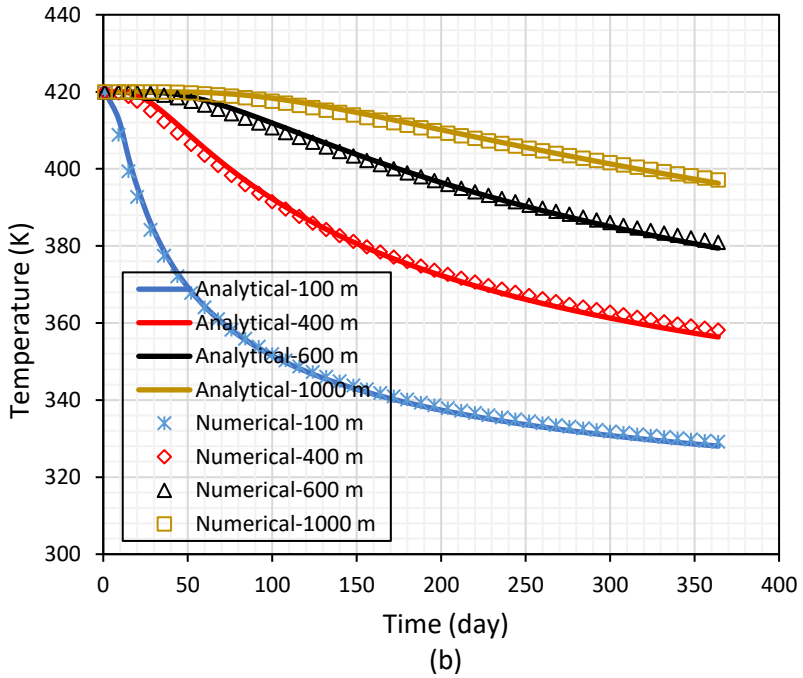

Fig. 3. Numerical results against analytical solution of the fluid temperature at (a) various times and (b) different positions along the fracture embedded in the rock.

Finally, the analytical solutions established for the drained and undrained responses of crack to a normal stress loading are used to verify the numerical model in terms of poroelastic deformation. Sneddon, (1946) proposed the following analytical solutions for the pressure-related variations of crack normal opening under both drained and undrained conditions:

$$D_n(x) = \frac{2P(1-v_u)}{G}\sqrt{a^2-x^2} \tag{52}$$

$$D_n(x) = \frac{2P(1-v)}{G}\sqrt{a^2-x^2} \tag{53}$$

Here, P and G represent the pressure within the crack and the shear bulk modulus, a shows the crack half-length, and finally v_u, and v and v_u denote the drained and undrained Poisson's ratio, respectively. Eq. 52 is proposed to evaluate the crack response to pressure loading under undrained conditions, while Eq. 52 corresponds to drained conditions. The geometrical model of the pressurized crack and corresponding model parameters are depicted in Fig. 4. Same as the heat transport validation, fifty elements with the same lengths are used to discretize the crack with a length of 1000 meters. The pressure inside the fracture is fixed at 10 MPa with zero initial normal and shear stresses. Fig. 5 depicts the short-term and long-term behaviors of the fault described by analytical and numerical techniques. It is obvious that numerical solutions are

matched well with the closed-form solutions for both undrained and drained conditions. The undrained condition dominates crack opening at early times due to the low fluid transport between the crack and rock matrix. As the fluid diffuses more into the rock matrix, the induced normal displacement gradually increases with evolving the undrained behavior of the rock-crack system to the drained behavior. A greater crack opening in the drained conditions corresponds to a change in the characteristics of the poroelastic material, making it softer as a result of fluid diffusion. Hence, the long-term response of fracture to pressure loading should be modeled using the drained material properties as shown in Eq. 53. It is also worth noting that the magnitude of the fracture aperture in both drained and undrained conditions depends on the boundary conditions. As there is no initial normal stress acting on the fracture surfaces and the fluid pressure inside it is relatively high (10 MPa), high magnitudes of maximum fracture aperture are reasonable. In addition, a slight discrepancy is also observed for the numerical results near the crack edges, especially in the case of drained condition, which is due to assuming a constant variation of normal DD across the tip elements.

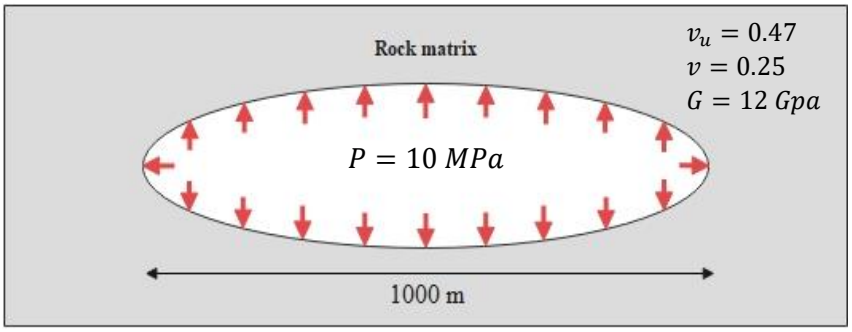

Figure 4. Schematic conceptual model of a single fluid pressurized fracture and corresponding model parameters.

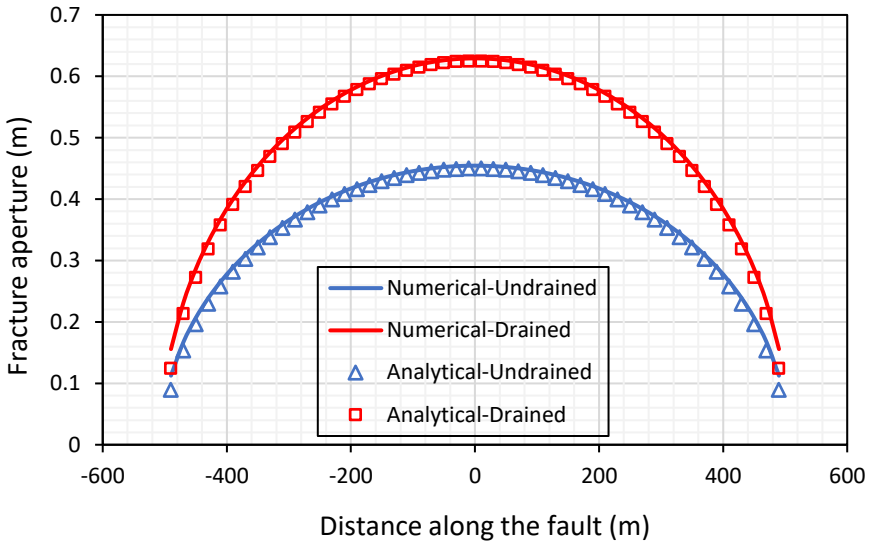

Fig. 5. Comparison of numerical and anlytical solutions for crack reponse to normal stress loading

4. Model setup

Here, strike-slip fault embedded in a horizontal 2-D and nearly impermeable rock matrix is considered. The rock matrix is as an unbounded porous, elastic and homogeneous medium, and the enclosed fault is modeled as a 1-D discontinuity. The fault has a length of 1000 m, and makes a 45-degree angle with the x-axis. We assess the fluid transport, heat transport, and rock deformation resulted from fluid injection at the center of the fault and analyze the process of induced seismicity as the pore pressure and cooling reduce the frictional resistance of the fault (Fig. 4). At the start of injection, in-situ stresses are anisotropic ($\sigma_x = 40\ Mpa$, $\sigma_y = 20\ Mpa$), and the initial pore pressure is zero. Here, water is the injection fluid a rate of flow equal to 10^{-4} $m^3 s^{-1}$ for each meter of the effective depth. Due to prevailing the plane strain condition in the z- direction, the effective depth of the fault is 1 m. Two injection temperatures are set in simulations $(300, 420\ K)$ to differentiate the temperature effect on dynamic instability. The mechanical properties corresponding to the porous medium are chosen based on experimental values measured for granite rocks, typical for deep Enhanced Geothermal Systems (EGS).

All model parameters corresponding to the rock, injection fluid, and fault have been summarized in Table 1. As discussed in section 2.7, the length of the steady sliding interface needs to be higher than the earthquake nucleation size, h^*, to generate dynamic events. In addition, the cohesive

zone size, Λ, which controls the numerical resolution during the rupture propagation, needs to be resolved with at least 3 to 5 spatial cell sizes. One way to address these issues is to sufficiently decreasing the cell size to meet the requirements of both resolution criteria, especially the cohesive zone size. But this approach is associated with significantly high computational cost and run time. As there is a positive correlation between the resolution criteria and the characteristic distance, the alternative approach would be setting larger values of D_c to produce dynamic events and reach sufficient numerical resolution with larger cell size. Although the characteristic distance is set to be a large value, it is in agreement with values found in laboratory studies (Marone, 1998). The reference velocity is chosen based on the value that is considered typical for relative plate motion (Almakari et al., 2019; Andrés et al., 2019; Cueto-Felgueroso et al., 2018; Pampillon et al., 2018).

As the Λ is the most restrictive condition for spatial discretization of the fault surface, resolving this criterion with sufficient cells is important to reach a proper numerical resolution during the dynamic rupture propagation. Day et al., (2005) suggested that Λ needs to be resolved with at least 3 spatial cells for achieving resolution-independent results and resolving the dynamic ruptures. In this study, we use 250 elements with the same lengths to discretize the fracture surface, corresponding to resolving h^* and Λ with 10.47 and 5.89 cells, respectively. So, based on the chosen rate-and-state parameters and boundary conditions, the mesh size used in this study is sufficiently low to observe nucleation of fault rupture.

We display the profiles of kinematic and dynamic parameters across the fault and assess their variation at five selected points (P1-P5) to characterize the fault response to the monolithic injection. Simulations are performed for 90 days divided into a number of variable time steps. The size of time step is calculated based on Eq. 46 to simulate long-term quasi-static deformation followed by fast aseismic slips. Therefore, relatively large time steps are used to simulate the quasi-static deformation within interseismic periods to reduce the computational cost associated with numerical solution algorithm. But dynamic ruptures are simulated with significantly smaller time steps to achieve a good numerical resolution. Simulations were carried out in parallel on MATLAB software using a high-performance computing (HPC) system with 32 logical processors and 64GB memory. Each time step includes manipulating approximately six billion data, and

about 10000 variable time step is required to resolve dynamic ruptures at each cycle. The model run time is inherently dependent on boundary conditions and user-defined size of time steps. For the prescribed model parameters, the corresponding processing time is about 6 hours.

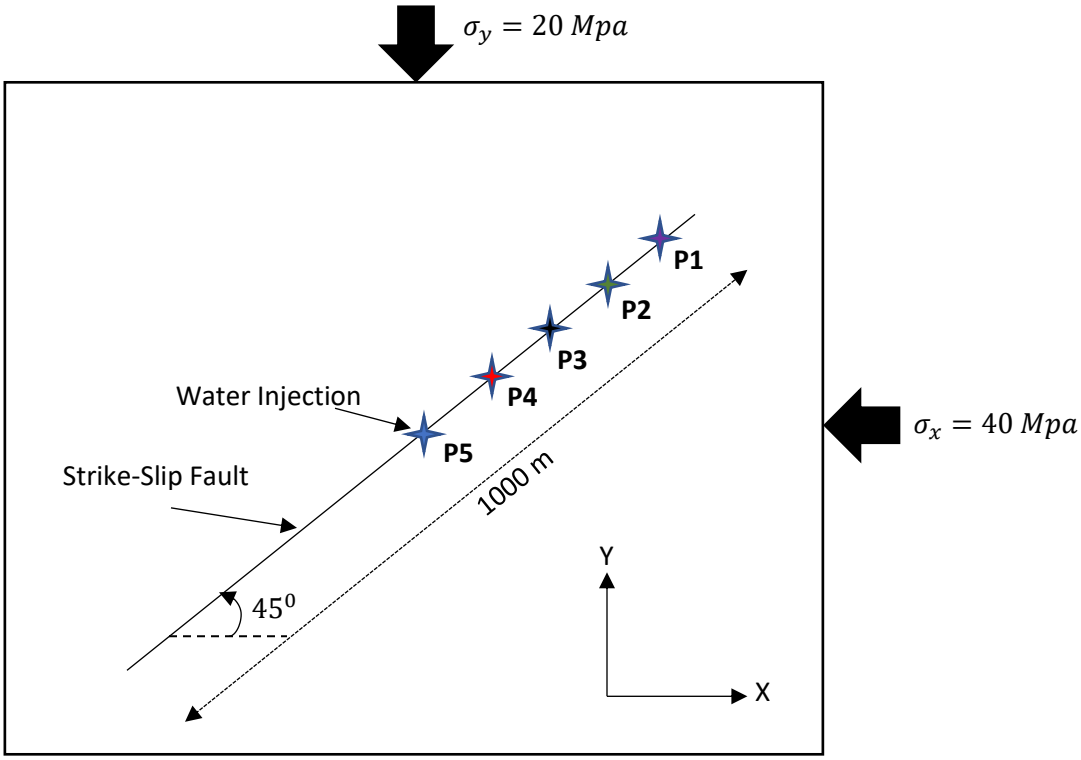

Fig. 6. Schematic of strike-slip fault with five selected points to evaluate the fault frictional behavior in response to non-isothermal water injection. The distances of P1, P2, P3, P4 and P5 (injection point) from the fault center are 400, 300, 200, 100 and 0 m, respectively.

Table 1. Model parameters for rock, fluid, and fault

Model Parameters: Rock Mass		**Model Parameters: Injection Fluid**	
Poisson ratio	0.25	Fluid density $\left(\frac{Kg}{m^3}\right)$	1000
Undrained Poisson ratio	0.47	Fluid viscosity $(Pa.s)$	0.001
Young modulus (GPa)	30	Fluid thermal conductivity $\left(\frac{W}{m.K}\right)$	0.6
Shear modulus (GPa)	12	Linear thermal expansion of the fluid (K^{-1})	10^{-4}
Skempton's pore pressure coefficient	0.86	Specific heat capacity of the fluid $\left(\frac{J}{Kg.K}\right)$	4200
Intrinsic Permeability (m^2)	10^{-15}	Injected fluid temperature (K)	300, 420
Biot coefficient	1	Injection rate $\left(\frac{m^3}{s.m}\right)$	10^{-4}
Rock density $\left(\frac{Kg}{m^3}\right)$	2700	**Model Parameters: Fault**	
Porosity	0.01	Reference friction coefficient	0.6
Rock thermal conductivity $\left(\frac{W}{m.K}\right)$	3.6	Reference slip velocity $\left(\frac{m}{s}\right)$	10^{-9}
Linear thermal expansion of rock (K^{-1})	7.9×10^{-6}	Characteristic distance (m)	0.001
Specific heat capacity of rock $\left(\frac{J}{Kg.K}\right)$	774	Rate-and-State parameters	$a = 0.01$ $b = 0.02$
Initial reservoir temperature (K)	420		
Initial reservoir pressure (MPa)	0	Initial normal stiffness $\left(\frac{GPa}{m}\right)$	20
In-situ stress in the X direction (MPa)	40	Initial shear stiffness $\left(\frac{GPa}{m}\right)$	20
In-situ stress in the Y direction (MPa)	20	Initial aperture (m)	10^{-4}
		Dilation angle (degree)	3

5. Results and discussion

5.1 Quasi-dynamic isothermal simulation of Injection-Induced seismicity

Fig. 7 shows the profiles of slip velocities for the selected points for five stick-slip cycles. Time is re-scaled to zero as the slip velocity exceeds 0.001 m/s at any particular point along the fault to depict the evolution of slip rate during the rupture propagation. It is noticeable that fault reactivation does not occur with a constant slip rate, and the magnitude of slip rate highly depends on the distance from the injection point and the number of previous seismic events. The slip velocity of the injection point (P5) is the lowest one during the first event. As rupture propagates towards the fault tip, slip velocity increases (to values more than 1 m/s) and reaches 4.65 m/s at P1 at 100m distance from the fault tip. This is because the rupture propagation velocity accelerates from the injection point toward the fault tips, leading to an increment of slip velocity. The radiation damping term controls the acceleration of the slip rate along the fault. Although acceleration of rupture propagation causes an increase in the slip velocity, it shortens the time interval during which the slip velocities of the points close to the fault tip remain within the seismic range.

The overall trends corresponding to the next four seismic events (b to e) are nearly the same, but they also have some differences in terms of the maximum slip velocity, velocity profile, and duration of slipping with seismic velocity. The second event occurs approximately after 25 days, with a maximum slip velocity of 2.78 m/s at P1. Slip velocities of other selected points (P2-P5) are also lower than those in the first event. This reduction in the peak slip rates can be largely attributed to the temporal variation of the effective normal stress and static shear stress, due to the monotonic fluid injection and dynamic ruptures, respectively. The magnitudes of the effective normal stress and shear stress applied on the fault surface govern the slip velocity and consequently seismic energy release during a particular seismic event. In the following sections, it will be shown that with a significant reduction of these kinematic parameters, slip rates do not exceed the aseismic range, and dynamic instability will no longer occur.

Further analysis of the velocity profile of other seismic events reveals that the peak slip velocity of the injection point (P5) is delayed in comparison with other monitoring points. This indicates aseismic slip (quasi-static deformation) prior to nucleation of a dynamic instability, leading to a gradual drop in the background shear stress and effective normal stress. As a result, not only the injection point does not experience a significant slip rate, the peak slip velocity of this point is also delayed compared with other monitoring points due to significant energy loss during the aseismic slip. In other words, prior to the onset of a dynamic instability, the difference between effective normal stress and shear stress strongly governs the amount of slip velocity and the time at which peak slip velocity manifests for a particular point. As it can be observed in Fig (7-d), for the fourth event, the peak slip velocity corresponding to monitoring points P5-P4 are also associated with delays in comparison with points P3-P1. This phenomenon is attributed to a reduced amount of shear and effective normal stress applied to those monitoring points prior to rupture nucleation.

In addition, Fig. 8 depicts the changes in slip velocity during the first rupture propagation to provide better insight into the evolution of slip velocity profiles. Once the length of the steady sliding interface exceeds the earthquake nucleation size, h^*, dynamic instability occurs, manifesting as rupture propagation towards the fault tip. As the rupture propagates towards the fault tip, slip velocity increases and reaches its maximum value at a point 52m away from the fault tip. Then, slip velocities follow a sharp decreasing trend, reaching 1.65m/s at the first nodal point which is 4m away from the fault tip. This indicates that rupture propagation speed accelerates till a specific point on the fault and then decelerates for rest of the fault, leading to not continuously increasing slip velocity over the fault. Therefore, if we place a monitoring point exactly at tip of the fault, relatively low slip velocity would be observed. Furthermore, a prolonged fluid injection results in a longer seismic duration (the time period at which slip rates are in the order of meters per second, elasto-dynamic range) and generally smaller but still seismic slip rates.

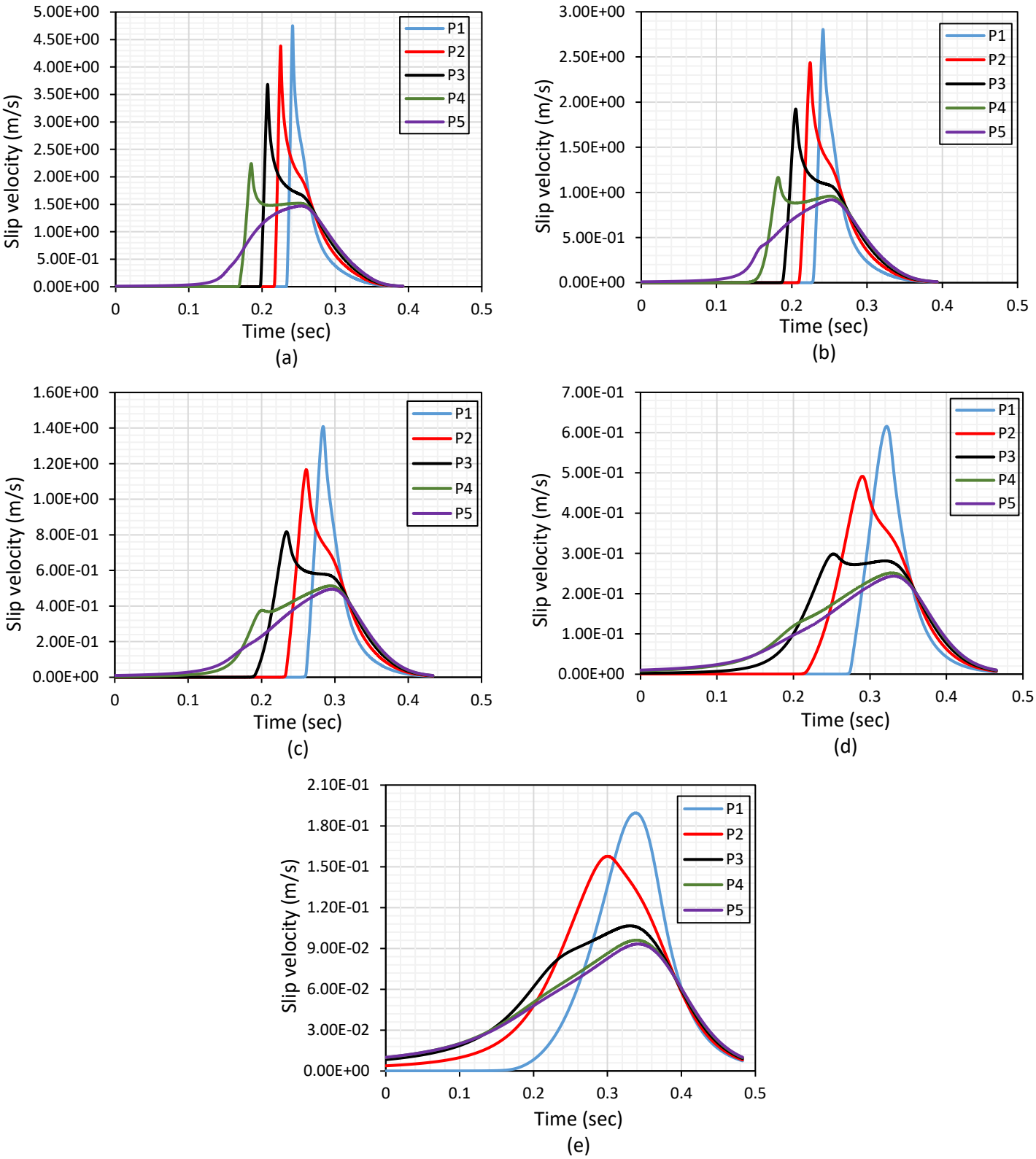

Fig. 7. Variation of slip velocity at five selected points for the (a) first event; (b) second event; (c) third event; (d) fourth event; and (e) fifth event. Time is re-scaled to depict changes in the slip velocities once the dynamic instability occurs.

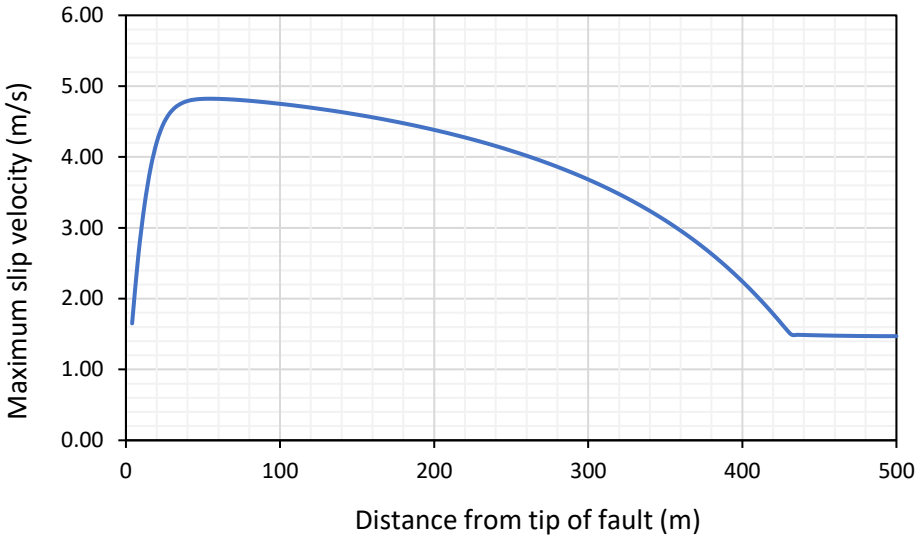

Figure 8. Slip velocity profile along the half length of fault during the first seismic event

Earthquake nucleation size prior to the onset of each dynamic event is shown in Fig. 9. The corresponding number of spatial cells resolving each nucleation size is also depicted in Fig.9. With increasing the number of events, the earthquake nucleation size increases due to decreasing the effective normal stress applied on the fault surface, reaching 228.53m prior to nucleation of last seismic event. Correspondingly, the number of spatial cells resolving each nucleation size increases from 17.32 spatial cells to 57.13 spatial cells, indicating that nucleation sizes are resolved with sufficient elements to observe the seismic events and reach sufficient numerical resolution.

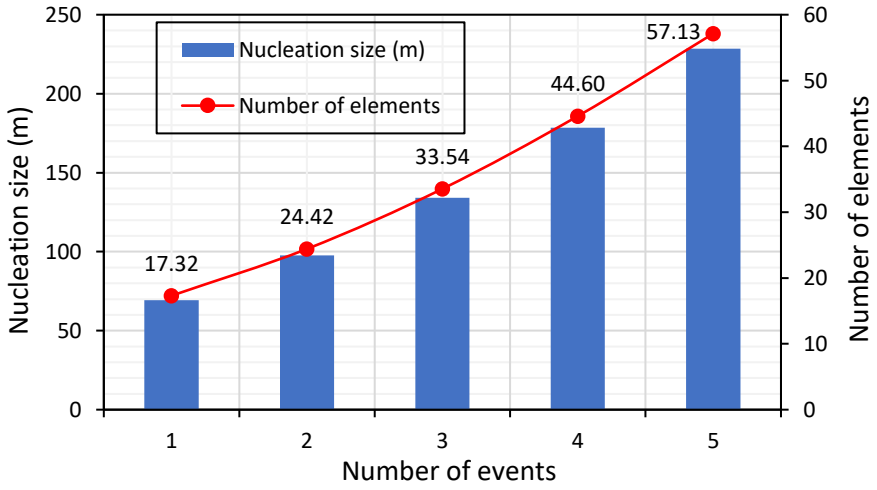

Figure 9. Earthquake nucleation size (h_RR) along with number of boundary elements resolving this length scale.

Fig. 10 shows the shear stress as a function of time during the seismic events for five selected points along the fault. The time is re-scaled to zero as the slip velocity exceeds 0.001 m/s at any particular point along the fault. As shown in Fig. 9(a), dynamic rupture starts to propagate from point P5, where the shear stress level before the dynamic instability significantly differs from its initial value (far-field stresses). As mentioned previously, an earthquake develops only if quasi-static deformation within the interseismic period develops beyond nucleation size, h^*. Hence, points along the fault with a distance from the injection point of less than h^* experience aseismic slips prior to a full seismic event, leading to a gradual drop in the shear stress as well as the seismic energy. These points do not experience significant peak strength and shear stress drops due to the significant energy loss during aseismic slip. Similar patterns can also be seen during the next four seismic events (b to e) for point P5, except that the temporal variation of shear stress becomes less significant as the number of seismic events increases. The peaks in shear strength are due to peaks in friction coefficient prior to the onset of dynamic instability (Fig.14) and manifest once dynamic rupture reaches a specific point along the fault. In other words, these peaks in shear stress show the time duration prior to nucleation of dynamic rupture, and their values are proportional to the rupture speed, slip velocity, and background normal and shear stresses. On the one hand, a higher rupture speed leads to higher peak strengths, and causes more significant stress drops during dynamic instability.

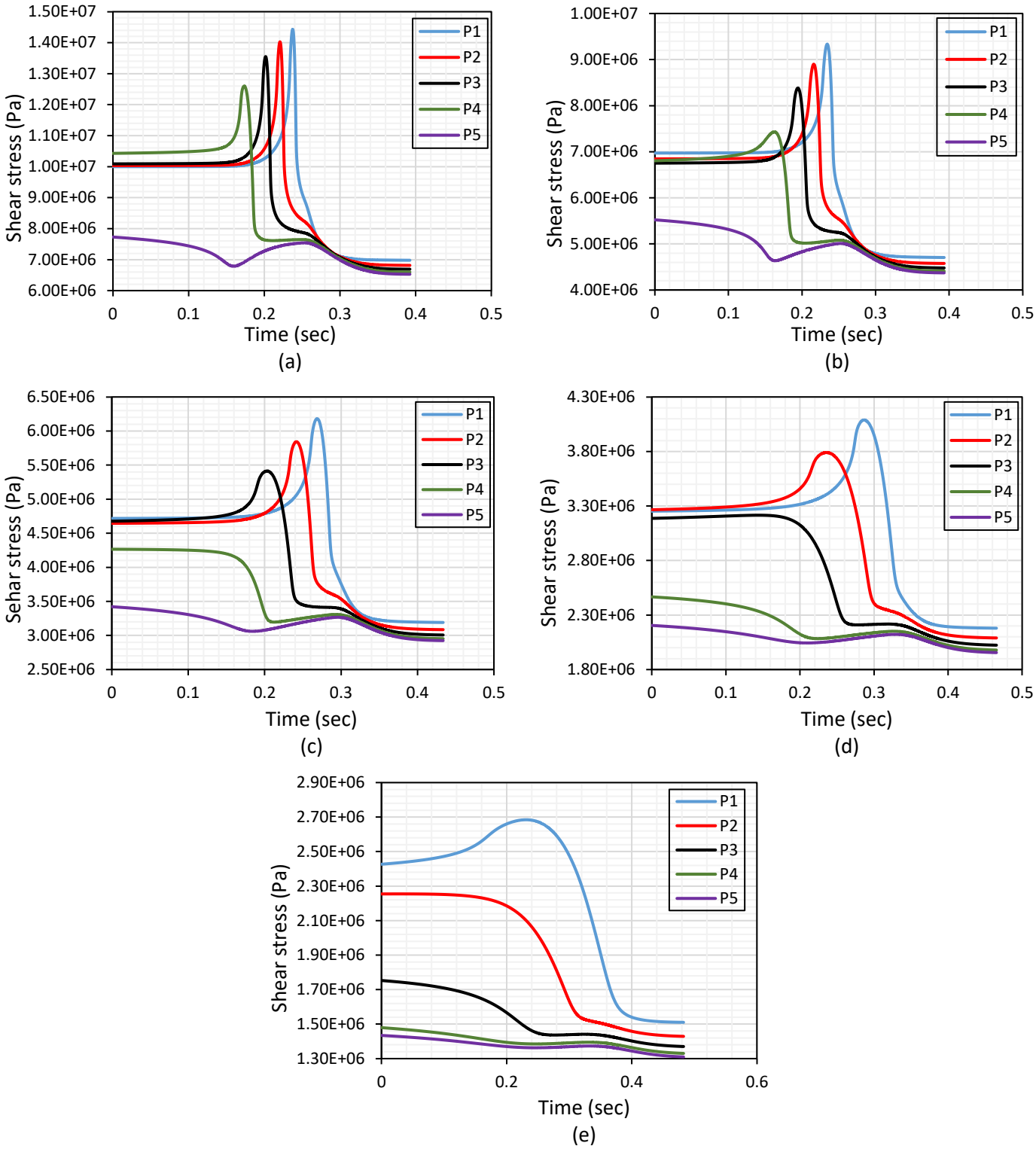

Fig. 10. Shear stress profile as a function of time at five selected points for the (a) first event, (b) second event, (c) third event, (d) fourth event, and (e) fifth event. Time is re-scaled to depict changes in shear stress once the dynamic instability occurs.

Hence, points located near the fault tips would experience higher stress peaks before dynamic instability and more severe stress drops during the seismic slip. On the other hand, the rise in the shear stress prior to the nucleation of dynamic rupture and the drop in the shear stress during the dynamic instability decay with increasing number of seismic events (Fig.10-a-e). As shown for the last seismic event (Fig. 10(e)), the shear stresses corresponding to points P2-P5 do not experience any peak shear strength, and all selected points experience significantly lower stress drops during rupture nucleation as compared to the previous seismic events. The amount of static stress drop correlates to the seismic energy released during nucleation of a dynamic instability. Therefore, the static stress drop is lower in the subsequent events because the fault has already slipped, and most of the seismic energy is released in the first event(s).

Fig. 11 shows the accumulation of shear displacement during each seismic event. Fault slip manifests as a succession of seismic slip events, separated by interseismic periods at which the quasi-static deformation dominates fault frictional behavior. Although the points near the fault tips are associated with higher slip velocities and more severe stress drops, they experience lower shear displacements during both seismic and interseismic periods, compared to the points located near the injection point. Comparison of slip accumulation during the five seismic events under investigation also reveals that the increments of shear displacement at the five selected points decay as the injection proceeds, being more significant for the points located near the center of the fault. This means that the induced shear displacement during each seismic event follows a decreasing trend over time, becoming less significant as the number of seismic events increases. Similar to the case of slip rate and shear stress profiles, there is also a negative correlation between slip increment and the number of seismic events, which can be mainly attributed to the interaction of the effective normal stress and the shear stress acting on the fault surface. The critical values of these parameters can be determined for a fault with the prescribed geological conditions, below which no seismic slip happens, and aseismic slips govern the unstable behavior. In addition, during the interseismic periods, most of the fault segments remain locked except for the points close to the center of the fault. These points (P1-P3) experience a limited amount of aseismic slip during time intervals bounded by two seismic events.

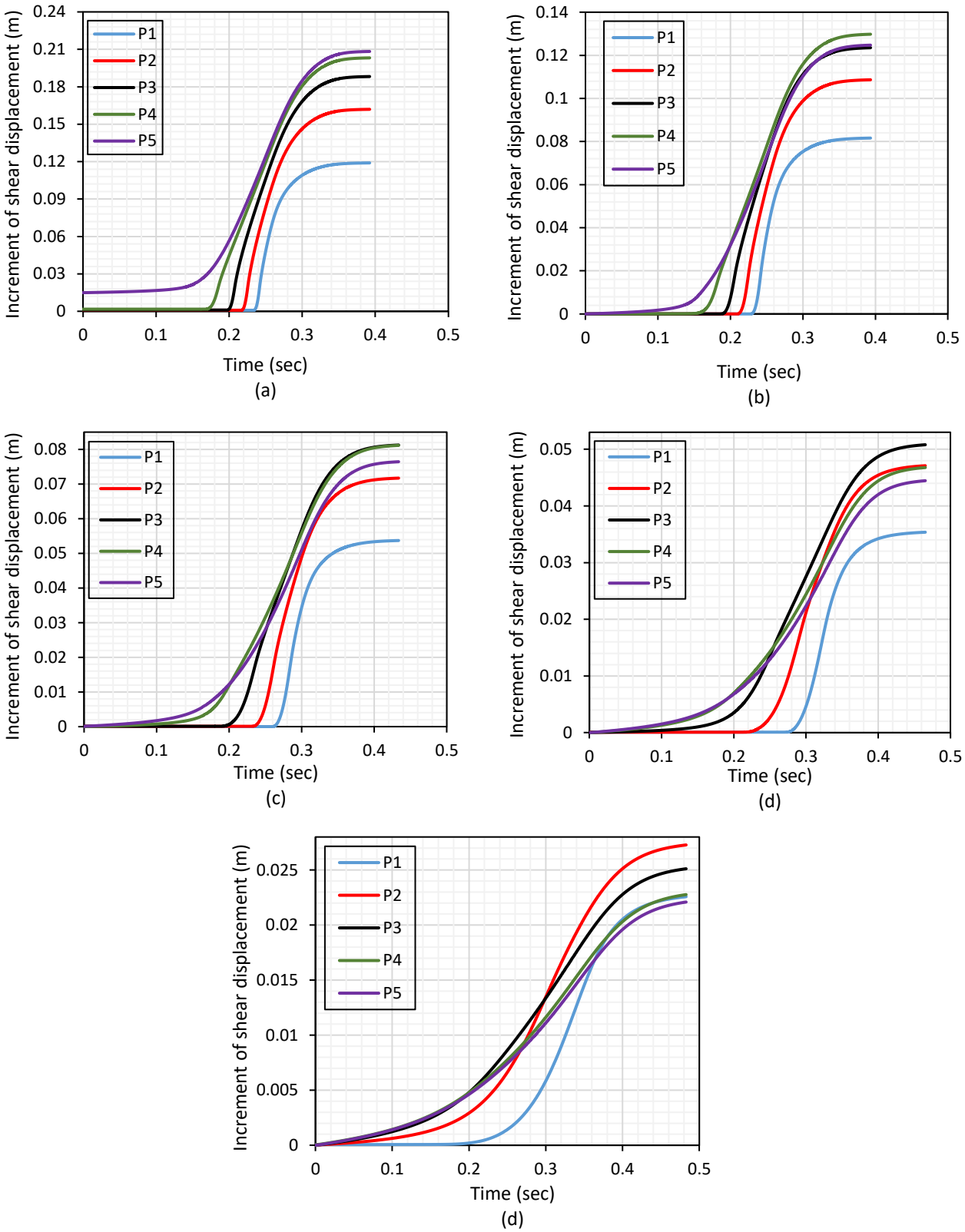

Fig. 11. Variation of shear displacement at five selected points for the (a) first event, (b) second event, (c) third event, (d) fourth event, and (e) fifth event. Time is re-scaled to depict changes in shear displacement once the dynamic instability occurs.

This aseismic slip that occurs along the fault with a size of h^* is necessary for the nucleation of dynamic rupture and the onset of an earthquake.

Analyzing the variation of shear stress as a function of seismic slip is of interest when assessing the slip-weakening effect. The stress-slip dependencies of the selected points for each seismic event have been shown in Fig. 12. Regarding the first event (Fig. 12(a)), shear stress reaches its peak value during a minor slip just before the nucleation of dynamic rupture. As dynamic instability occurs, the stress-slip dependence can be generally categorized into three linear parts with different slopes (Fig. 12(a)). The first part is where the shear stress reduces with a steep slope relative to the shear displacement, and the slip rate is in the seismic range. In the following sections, we will refer to the slope of this part as the slip-weakening rate. In the second part, shear stress variation relative to the seismic slip is significantly reduced, but the slip velocity is still in the seismic range. In the last part, the stress-slip dependence continues with a steeper slope than the previous part, with a slip rate out of the seismic range. Regarding point P5, stress-slip dependence is not similar to the four other selected points, due to aseismic slips prior to the fully seismic event. The five selected points (Fig. 12(a)) exhibit a stress-slip dependency that closely follows the linear slip-weakening law. This law describes the linear reduction of the shear stress relative to slip increment based on slip-weakening rate W:

$$W = -\frac{d\tau}{d\delta} \approx \frac{b\sigma}{D_c} \tag{54}$$

The above equation can only be applied to the first part. The slip-weakening behaviors of these points are almost similar, but not same, indicating that slip-weakening distance and peak shear stress increase as rupture propagates along the fault. The observed increase in the prescribed parameters is because the rupture propagation slip increases as it progresses along the fault, and the corresponding rise in propagation slip leads to higher values in slip-weakening distance and peak shear stress. These results also confirm the findings of a previous research (Lapusta & Liu, 2009), in which a fully dynamic modeling was applied to simulate fault reactivation under tectonic loading. Analyzing the stress-slip profile of the next events (Figs. 12(b) to (e)) reveals that at each particular seismic event, all curves start and end at different slip levels. As shown before, each point along the fault experiences different levels of shear displacement during a particular dynamic instability. As the sliding history differs from one point to another along the fault, the

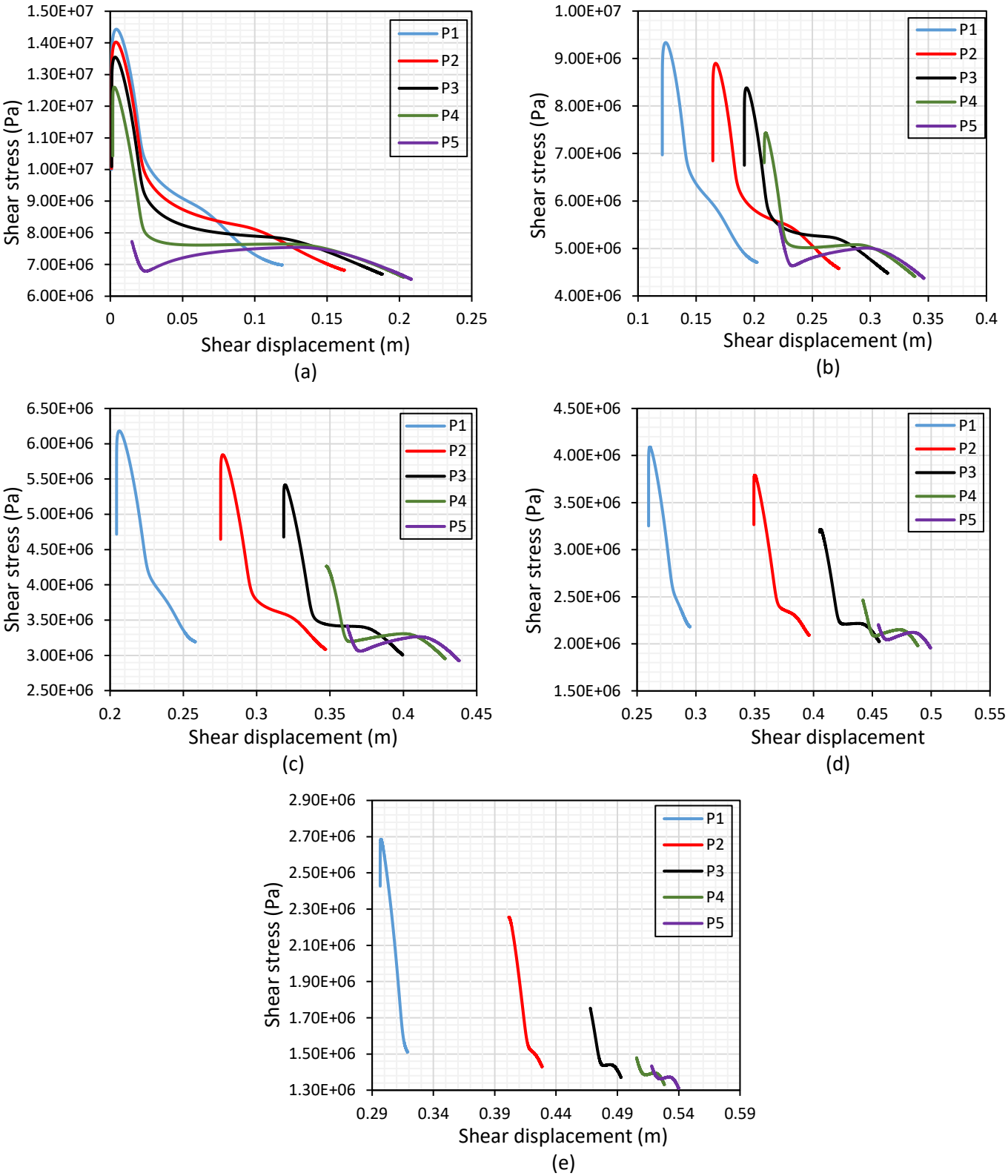

Fig. 12. Shear stress-slip profile at the five selected points during the (a) first event, (b) second event, (c) third event, (d) fourth event, and (e) fifth event. Time is re-scaled to depict changes in the shear stress-slip dependence once the dynamic instability occurs.

stress-slip profiles of the points are associated with different start and endpoints for the subsequent events. A more detailed analysis of the stress-slip profiles also shows that the slip-weakening rates at all selected points gradually decrease with an increase in the number of stick-slip cycles. This can be attributed to the reduced effective normal stress applied on the fault surfaces due to the continuous fluid injection. The slip-weakening law is based on the rate-and-state friction law with some simplifying assumptions. This law only applies to dynamic rupture propagation where slip velocity is relatively high, being in the seismic range. In many studies, the slip-weakening law (Eq. 54) is used to capture the frictional behavior of natural fractures or faults with prescribed peak shear strength and residual shear stress, leading to unrealistic results. As shown in Fig. 12, the peak shear strength, residual shear stress, and effective slip-weakening distance are not constant along the fault. They vary from one seismic event to another and highly depend on the fault properties and geological boundary conditions.

Fig. 13(a) shows the seismic moment (red line), moment magnitude (blue line), and seismic energy (green line) yielded by each dynamic instability as a function of the total injected volume. These parameters are computed for each seismic event in a time interval at which the slip velocity on the fault stays above 0.001 m/s, which is the seismic velocity threshold. The velocity threshold is set low enough to ensure that each dynamic instability is evaluated during the whole seismic time. Since the developed model is 2-D (plain strain in the z-direction), the measured seismic moment, moment magnitude, and seismic energy are determined per meter of the strike-slip fault length. Obviously, the seismic moment released in each seismic slip follows a decreasing trend as the injection proceeds. The first seismic event occurs 10.2 days after injection, with a seismic moment of $1.9 \times 10^{12}\ N.m$ per meter of the effective depth, and the last event takes place 67.2 days after injection, associated with $2.7 \times 10^{11}\ N.m$ seismic moment per meter of the effective depth. Fig. 13(a) also shows a declining trend for the moment magnitude, with values of 2.11 and 1.55 at the first and last events, respectively. It has been previously reported that the total injection volume is directly proportional to the number of seismic events and the released moment magnitude (Galis et al., 2017; McGarr & Barbour, 2018; Van der Elst et al., 2016). However, our simulations show a negative correlation between the total volume of the injected fluid and the seismic magnitude. The main difference between our results and field

observations on the seismic magnitude-injected volume relationship is that we are looking at only one single fault, but in the field, more and more faults are pressurized with continuous injection. Considering a single fault with prescribed rate-and-state parameters, the seismic energy released during a particular event is completely dominated by the values of the effective normal and static shear stresses prior to the nucleation of that dynamic instability.

For quantitative interpretation, the absolute difference of these kinematic parameters, represented by parameter Δ, is computed prior to each dynamic rupture, as shown in Fig 13-b as a green line. Obviously, the value of Δ becomes lower with increasing the injected fluid volume, decreasing from 6.4 MPa to 1.3 MPa before the onset of the first and last seismic events, respectively. This suggests that the negative correlation between the seismic energy and injected volume can be attributed to the variation history of Δ on the fault surface, such that decreasing Δ reduces the released seismic energy as well as the moment magnitude. For the prescribed model parameters, the critical value of Δ is about 1.3 MPa, below which slip accumulation occurs as an aseismic slip.

Interestingly, further simulations showed that that number of seismic events is limited and variable depending on the geological boundary conditions and fault characteristics. In our simulations, five seismic events were observed, but a different number can be detected for a field with different geomechanical characteristics. Irrespective of the number of seismic events, seismic slip would no longer occur as there is a significant seismic energy release in the previous events, leading to quasi-static deformation during the rest of the injection time. It is worth noting that the moment magnitudes shown in Fig. 13(a) are associated with the seismogenic region with 1000 m length and 1 m width due to the plane strain assumption. For a seismogenic region with 1000 m width, the associated moment magnitude would be 4.11 for the first event, corresponding to a seismic moment of $1.9 \times 10^{15}\ N.m$. This indicates that destructive earthquakes are inevitable if a large portion of fault is exposed to fluid overpressure. The average slip yielded by each seismic event is depicted in Fig. 13(b). The average slip associated with the first event is 0.158 m, which nonlinearly decreases to 0.022 m during the fifth event.

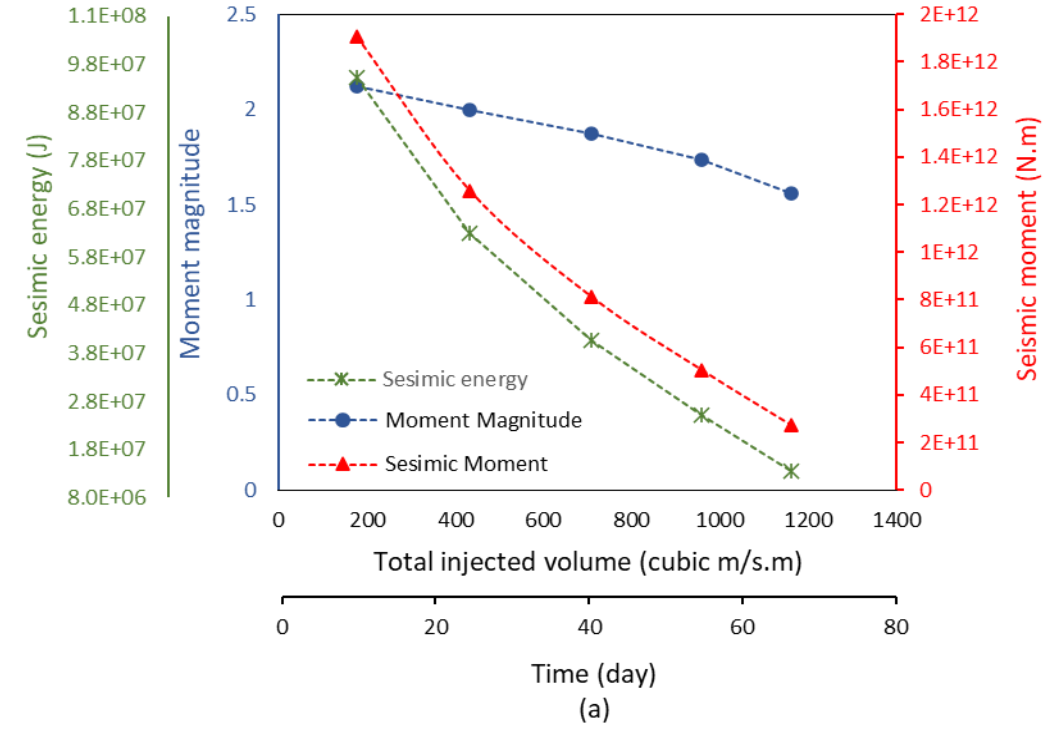

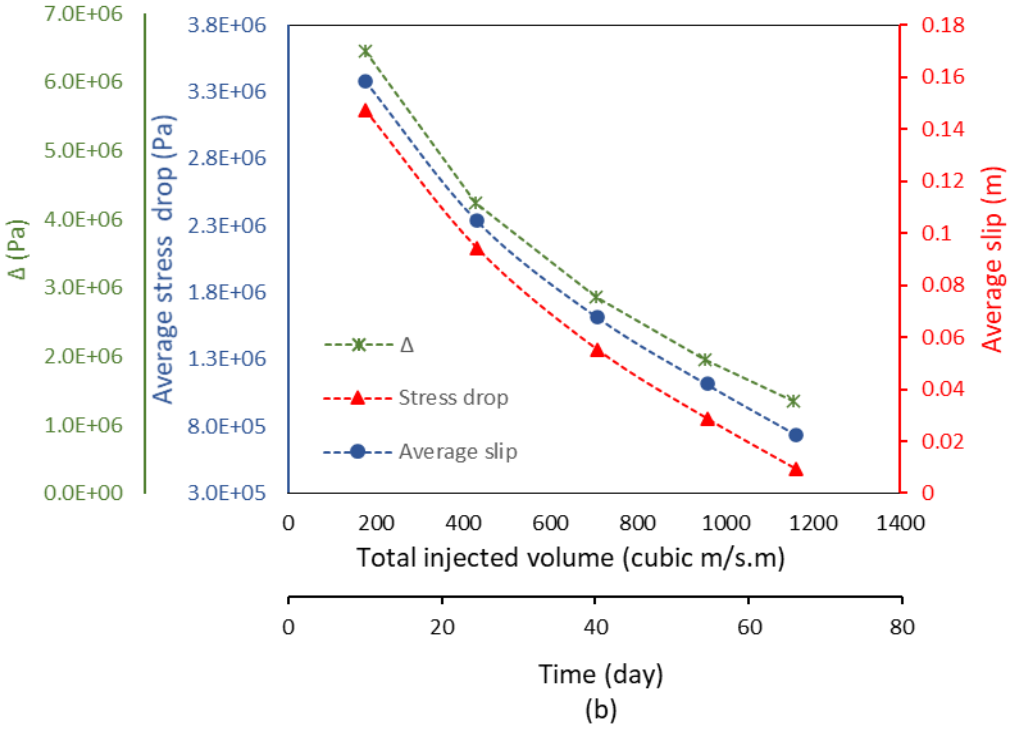

Fig. 13. Variations of the seismic moment, moment magnitude, average slip, and static stress drop as functions of the cumulative injected fluid volume.

The shear stress drop and the cumulative injected fluid are also shown as functions of time in Fig. 13(b). The static stress drop $\Delta\tau$ can be computed as follows:

$$\Delta\tau = \bar{\tau}(t_{ini}) - \bar{\tau}(t_{end}) = \frac{1}{|\Gamma|}\int_{\Gamma} \tau(x; t_{ini}) d\Gamma - \frac{1}{|\Gamma|}\int_{\Gamma} \tau(x; t_{end}) d\Gamma \quad (55)$$

Where Γ is the seismogenic region (with a velocity-weakening frictional behavior) and t_{ini} and t_{end} are the time points for a particular seismic event, in which the peak slip rate on the fault is higher than 0.001 m/s. The static stress drop is approximately 3.1 MPa during the first seismic event, reaching about 4.8 Pa during the last event. Comparing Figs. 13(a) and 13(b) also confirms that large static stress drops are associated with earthquakes with higher moment magnitudes.

The evolution of Coulomb failure stress (CFS) and friction coefficient for point P5 are shown as functions of time in Fig. 14. Prior to nucleation of the first dynamic instability, CFS exhibits an increasing trend as the injection proceeds and reaches a positive value after 8.66 days, when the aseismic slip begins. Interestingly, the aseismic slip or creep is associated with a gradual increase in the friction coefficient and a negligible rise in CFS. The quasi-static slip lasts for about 1.6 days with a slip velocity of the order of 10^{-6} m/s prior to the first dynamic instability. Then, CFS suddenly increases to a peak value of 1.38 MPa, just before nucleation of the first dynamic rupture, followed by a sudden decrease during the seismic slip.

The peak value of the friction coefficient prior to nucleation of dynamic rupture is 0.62, indicating that the fault is reactivated at a friction coefficient higher than that under static conditions. The maximum and minimum values of friction coefficient are highly dependent on the rate-and-state parameters. Both CFS and friction coefficient follow an increasing trend during the interseismic period where the fault mainly remains locked, without any slip. The second aseismic slip begins once the CFS becomes positive, increasing very slowly during the aseismic slip and peaking suddenly to 0.69 Pa prior to the second seismic slip. On the other hand, the onset of the second aseismic slip is associated with a steeper increase in the friction coefficient similar to the first aseismic event, except that the second earthquake occurs at a lower value of friction coefficient (equal to 0.61) compare to that in the first event. Although similar trends corresponding to CFS and friction coefficient are also valid for the next three seismic events, the peak and trough values for CFS decay over time with increasing the number of seismic events. The last seismic event

occurs after 67.27 days of continuous injection, and then any change in the friction coefficient and CFS corresponds to an aseismic slip. In other words, after the fifth seismic event, slip rates stay below the elasto-dynamic range, and the slip increment manifest as a low-velocity process, aseismic slip, once the CFS becomes positive. Hence, the quasi-static slip completely dominates the fault frictional behavior after some injection time, while the friction coefficient converges to its steady-state value.

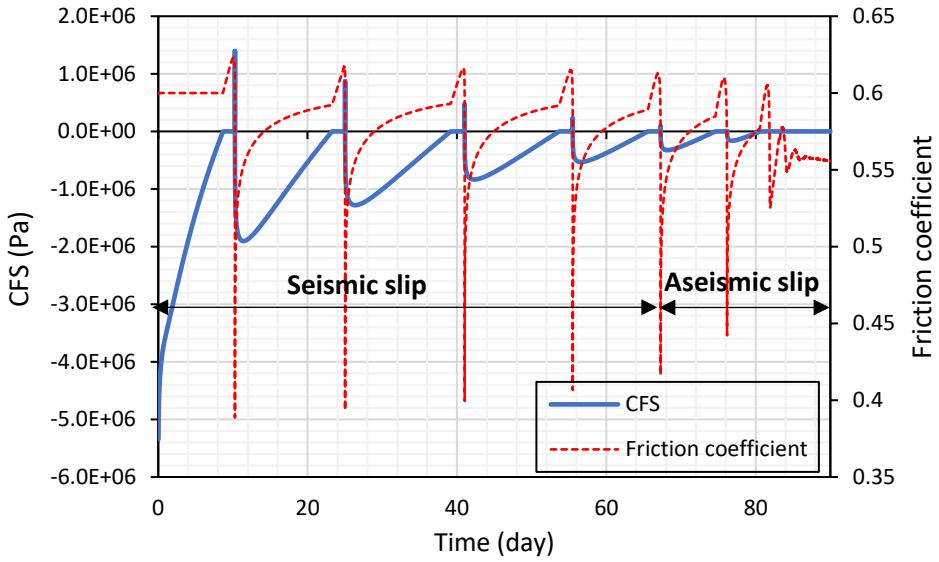

Fig. 14. Variation of the coulomb failure stress along with the friction coefficient at the center of the fault (P5) over time.

It is also worth knowing the impact of a seismic slip on the surrounding rocks. Fig. 15(a) depicts the evolution of the stress tensor in the x-y coordinates at the fault tip. The step-wise trends observed for stresses global coordinate result from the nucleation of dynamic instabilities. The stress measured in the x-direction decreases and becomes more compressive as a result of the seismic slip, but the stress in the y-direction follows an increasing trend and becomes more tensile in response to fault slippage. The significant reduction of S_{yy} at the fault tip lays as the main cause for fault propagation. The stress in the x-y plane follows a decreasing trend resulting mainly from fault deformation in the normal direction. This indicates that crack opening is a dominant factor in the temporal variations of S_{xy}, rather than slippage.

Fig. 15(b) shows the temporal variations of the stress tensor at a position 0.5 m above the injection point. Both S_{xx} and S_{yy} gradually decrease and become more compressive in response

to fluid diffusion and fracture normal displacement during the interseismic periods. As the rupture nucleates, S_{xx} and S_{yy} are affected as sudden rises and drops, respectively. Interestingly, the associated trends are the opposite of those observed at the fault tip. Regarding S_{xy} at the selected observation point, crack opening dominates the variation of this parameter over time again, without any significant contribution from slippage. In addition, the temporal variations of principal stresses equivalent to each stress tensor measured at the observation points have been shown in Figs. 15(c) to (d).

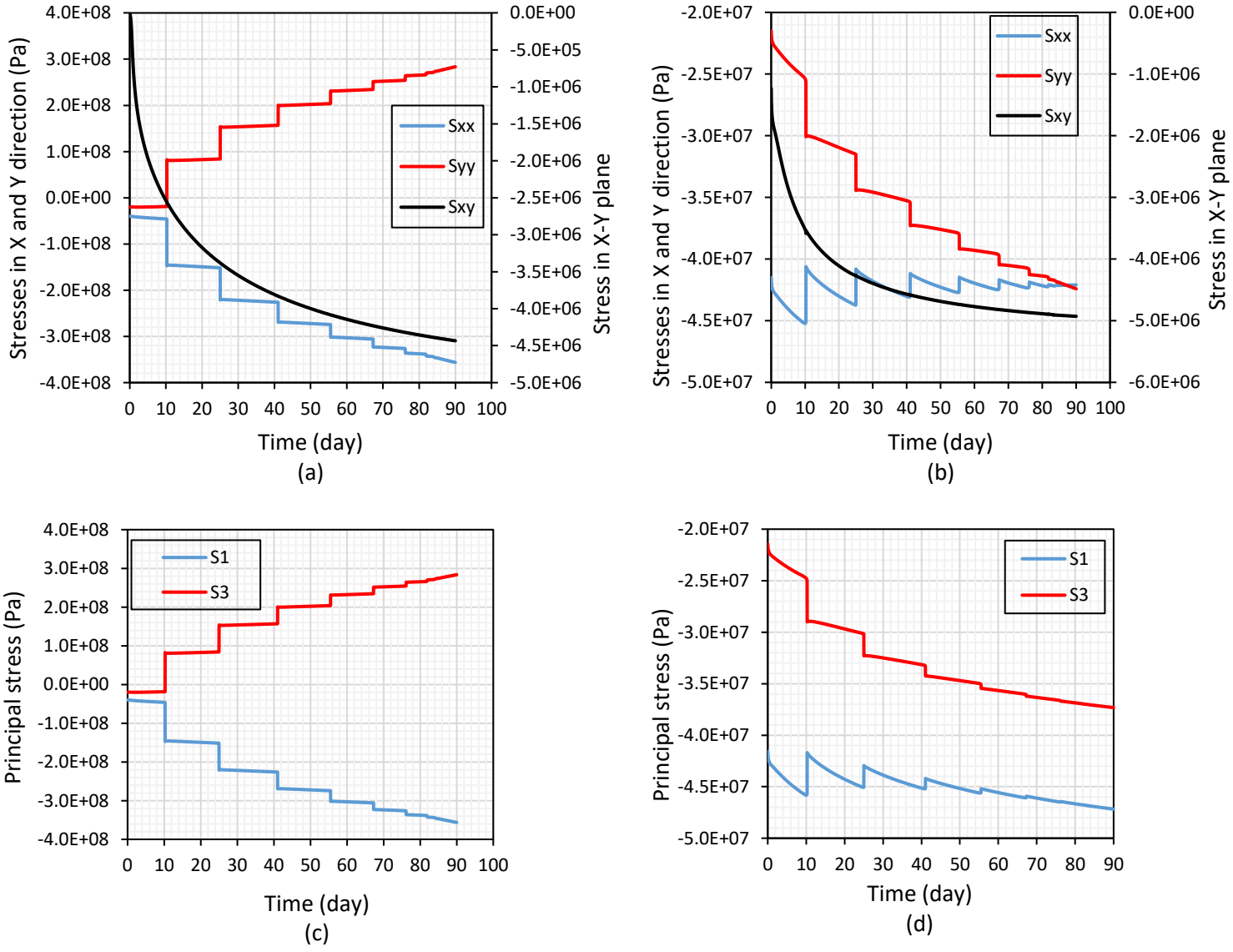

Fig. 15. Temporal variation of the stress tensor and principal stress (a) and (c) at the fault tip; (b) and (d) at a point 0.5 m away from the center of the fault, respectively

In overall, it can be seen that the contribution of the seismic slip for principal stresses measured near the fault tip is not comparable with that for the stresses evaluated near the fault center. Earthquake nucleation significantly affects the principal stresses near the fault tip, such that they follow a symmetric trend with respect to each other (Fig. 15(c)). It is worth noting that principal stresses at the fault tips are changing by about 300 MPa, which is not comparable with the initial principal stresses ($\sigma_x = 20\ Mpa$, $\sigma_y = 10\ Mpa$). This significant stress variation can be due to ignoring the fracture propagation once stress concentration around the fault tip satisfies the propagation criteria. In our study, fault is more likely to propagate in mode II due to the high values of shear displacements resulting from injection-induced seismicity. Our simulation results also confirm the potential of fault propagation, because the value of equivalent stress intensity factor exceeds the fault stiffness during nucleation of the first dynamic instability. Hence, neglecting fracture propagation on one hand and the effect of full seismic slips on the other hand, lead to severe increases in stress concentrations around fault tips. This is not the case for principal stresses measured near the fault center (Fig. 15(d)). At this observation point, the effect of seismic slips on the maximum principal stress is partly neutralized by the poroelastic deformation and fluid diffusion.

5.2 Controlled fluid injection to mitigate seismic risk

The results obtained for continuous fluid injection (Fig. 13) confirm that monotonic injection has the potential to cause anthropogenic earthquakes with considerably high seismic magnitudes. Despite inducing high slip values, this injection style is not proposed for permeability enhancement, too, as it rises major environmental concerns. Hence, cyclic injection may be the only applicable alternative to mitigate the associated seismic risks in underground fluid injection projects.

According to previous experimental studies, cyclic pressurization of fault in a permeable rock matrix promotes seismic slip rather than an aseismic one, owing to the increasing the fracture stiffness in response to the slip-rate perturbation (Noël et al., 2019). However, locally undrained conditions in in-situ fractures formed in low-permeable reservoirs may positively contribute to the stable and slow slippage (Ji, Zhuang, et al., 2021). To achieve this, the model parameters associated with the fault, rock matrix, and injected fluid are the same as those shown in Table 1,

except for the rock matrix permeability that was decreased by ten times to $10^{-16}\ m^2$. Four fluid injection schemes are modelled with the developed earthquake simulator, including the volume-controlled cyclic injection with and without backflow, stopping injection after reaching a certain moment magnitude (TLS without backflow), and backflow after detecting unstable conditions (TLS with backflow). In the volume-controlled cyclic injection without backflow (VC without backflow), water injection rate is $0.0002\ \frac{m^3}{m.s}$, and injection is terminated once the injection pressure reaches 97% of the bottom hole pressure where fracture fails with monotonic injection. For each cycle, 12 hours is considered for duration of shut-in stage. For the volume-controlled cyclic injection with backflow (VC with backflow), the bottom hole pressure is kept constant at atmospheric pressure for 12 hours after the injection pressure reaches the prescribed critical value. The corresponding termination criteria was designed based on a trial-and-error approach to reach the maximum value of injection pressure, at which stopping the injection would guarantee the quasi-static slip during the post-injection stage. Our simulations show that if a bit higher value is set as the peak injection pressure, cessation of injection would fail to prevent seismic slips in some cycles.

For the last two injection schemes, the criterion for injection termination is based on TLS, in which fluid injection continues until reaching a certain moment magnitude. TLS refers to the standard actions implemented for seismic risk management during the activities associated with forced-fluid injection. The magnitude level, seismic protocols and field operations are selected based on the type of activity such as re-injection or hydraulic stimulation. Fig. 16 shows an example of TLS designed for the soft stimulation treatment of well RV-43 in Reykjavik (Hofmann et al., 2021). For the third injection scheme (TLS-without backflow), the goal is to continue injection and allow the fault to be reactivated as quasi-static slips till the moment magnitude exceeds the critical value, and then stopping injection for a constant duration of 12 hours. For the last injection scheme (TLS-with backflow), the injection stage and criteria for termination of injection are similar to the case of TLS without backflow, except for the post-injection stage in which the well is allowed to backflow at a fixed bottom hole pressure of 0.1 MPa (atmospheric pressure).

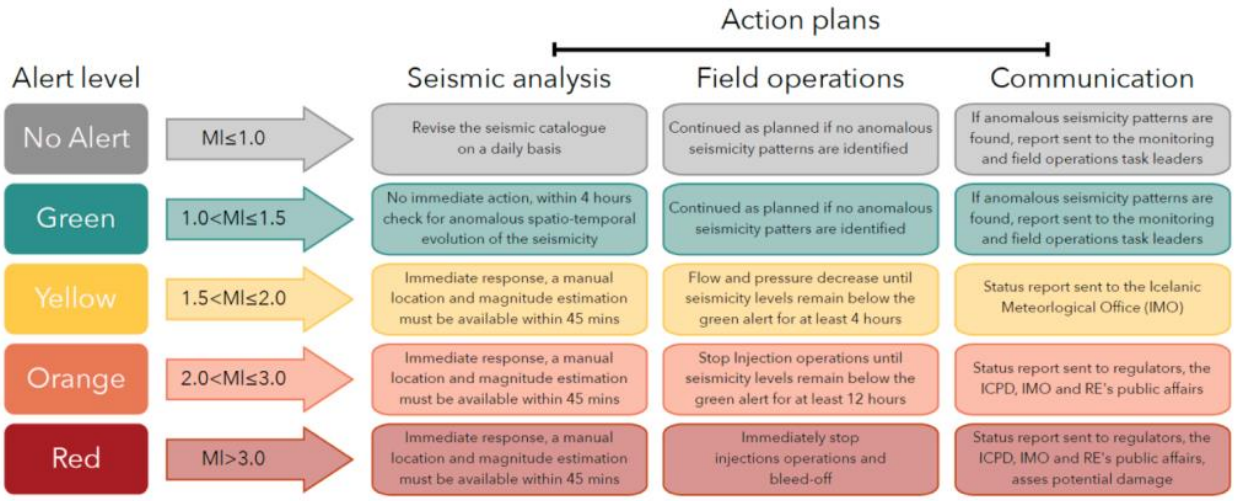

Fig. 16. An example of traffic light system (TLS) developed for the hydraulic stimulation of well RV-43 in Reykjavik (Hofmann et al., 2021).

It is worth noting that the upper and lower bounds of moment magnitude at each level of TLS systems cannot be exactly applied to 2-D problems, as the yielded moment magnitude is per 1-meter of the effective depth. In addition, termination of injection may not be able to prevent the nucleation of full seismic events, if the critical value of moment magnitude is not set properly. Hence, a number of simulations were conducted to reach a maximum value of moment magnitude (per 1-meter of fault width) with minimum seismic risk during the post-injection stage. Based on simulation outcomes, the critical moment magnitude was chosen to be -0.1, which is corresponding to $Mw = 1.5$ (the upper bound of the green level at TLS systems) in the field case assuming a fault/reservoir height of 250 m.

Fig. 17 shows the variations of injection rate and injection pressure for the four proposed injection schemes. For cyclic injection based on TLS-without backflow (Fig. 16(a)), each cycle is composed of two stages, namely injection stage and shut-in stage. The injection stage continues with a constant injection rate of $0.0002\ \frac{m^3}{m.s}$ till the moment magnitude exceeds the value of -0.1. Aseismic slips also occur at this stage, with slip rates below the seismic range. Following this, injection is terminated, and the shut-in stage begins for a constant duration of 12 hours. For this injection scheme, the injection rate takes the binary values of 0 and $0.0002\ \frac{m^3}{m.s}$ at each cycle. The bottom hole pressure (injection pressure) increases during the injection stage and decreases nonlinearly as the shut-in stage begins. At the end of shut-in stages, the pressure level decreases

with increasing the number of cycles, converging to 13 MPa after 30 days of injection. Duration of the injection stages also dwindles as number of cycles increases, indicating a uniform pressure distribution and homogenous effective normal stress drop along the fault. In the cyclic injection based on TLS-with backflow (Fig. 17(b)), injection is terminated and the bottom hole pressure is fixed at atmospheric pressure once the seismic magnitude reaches -0.1. The extraction rate corresponding to the shut-in stage gradually increases with increasing the cycle number. Except for the first cycle, the durations of the injection stages and maximum values of injection pressure experience almost no significant changes during the remaining 29 cycles. Overall, comparing Figs 17(a) to (b) reveals that backflow decreases the number of cycles and causes the maximum injection pressure to fluctuate within a relatively small range. In the volume-controlled cyclic injections (Figs. 17(c) to (d)), injection termination occurs once the injection pressure reaches a value equal to 97% of the fracture failure pressure. Except for the cycle numbers, the trends of other features of these injection schemes are approximately similar to those of the TLS-based injection schemes. The number of cycles for the injection schemes based on VC with and without backflow are 32 and 50, respectively. It is also worth noting that the extraction rates for cyclic injection based on TLS are relatively higher than those at injection scheme based on VC, being related to the maximum values of bottom hole pressure at which the injection is terminated.

Fig. 17 also shows the variations of shear displacements and slip rates as functions of time for point P5 in the proposed cyclic injection schemes. It can be generally seen that cyclic injection induces a piecemeal rise in shear displacement with slip velocities below the seismic range. Fault slip behavior can be characterized as acceleration and deceleration in each cycle, and the transformation from acceleration to deceleration manifests as peaks in the slip velocity. For the case of TLS without backflow, water is injected into the center of the fracture at a constant rate, and the fracture is allowed to slip until reaching a moment magnitude of -0.1. The first three cycles show relatively high peak slip rates, with the maximum peak slip rate of $2\ \mu m/s$ in the second cycle. Subsequently, the peak slip rates are mostly below $0.5\ \mu m/s$, except for those corresponding to four consecutive cycles in the middle of total injection time. For the TLS with backflow, the borehole pressure is reduced to atmospheric pressure once the moment magnitude reaches a value of -0.1. In this injection scheme, the third cycle yields a maximum slip

velocity of $6.5\ \mu m/s$, being three times greater than the highest peak slip rate in the TLS-without backflow. However, the rest of the cycles yield lower peak slip rates, indicating that the slip velocity of the fault is more restricted by fluid extraction during the post-injection stage. In the case of VC without backflow, each cycle includes water injection until reaching a bottom hole pressure of 97% of the injection pressure at fracture failure, and then stopping injection for a constant duration of 12 hours. The maximum peak slip rate ($0.15\ \mu m/s$) yielded by this injection scheme is significantly lower than those observed in TLS-based injection schemes. In this cyclic injection, the peak slip rates are not allowed to accelerate more during the injection stage, thus becoming comparable with the reference velocity (V^*) after 20 days of cyclic injection. This indicates that VC without backflow can be a viable alternative to the monotonic injection scheme in fields with the risk of anthropogenic earthquakes. For VC with backflow, the peak slip rates exhibit slightly different trends. The peak slip rate gradually increases and reaches a maximum value of 0.41 $\mu m/s$ after 11 days, which is 173% of that in the VC-without backflow. These results suggest that fluid extraction causes stable fault slippage with higher peak slip rates (below the seismic range, of the order of 10^{-7} m/s) for injection styles based on VC.

In the previous section, it was demonstrated that cyclic injection can be an effective injection approach for seismic risk mitigation. Despite reducing the seismic risk, stable and slow fracture slip is encouraged by cyclic injection which can be a viable alternative to enhance fault conductivity through shear stimulation. Fig. 18 shows the increase in the induced aperture as a function of time in the four studied cyclic injection schemes. For the cyclic injection based on TLS-without backflow, the increase in the fault aperture is much higher than those in the other three injection schemes. The induced aperture reaches approximately 6.3×10^{-4} m in the middle of injection time. Thereafter, it rises to about 8.8×10^{-4} m within three days, and then follows a linear trend for the rest of the time to finish at 1.13×10^{-3} m, being indicative of a more than ten times irreversible increase in the fault initial aperture.

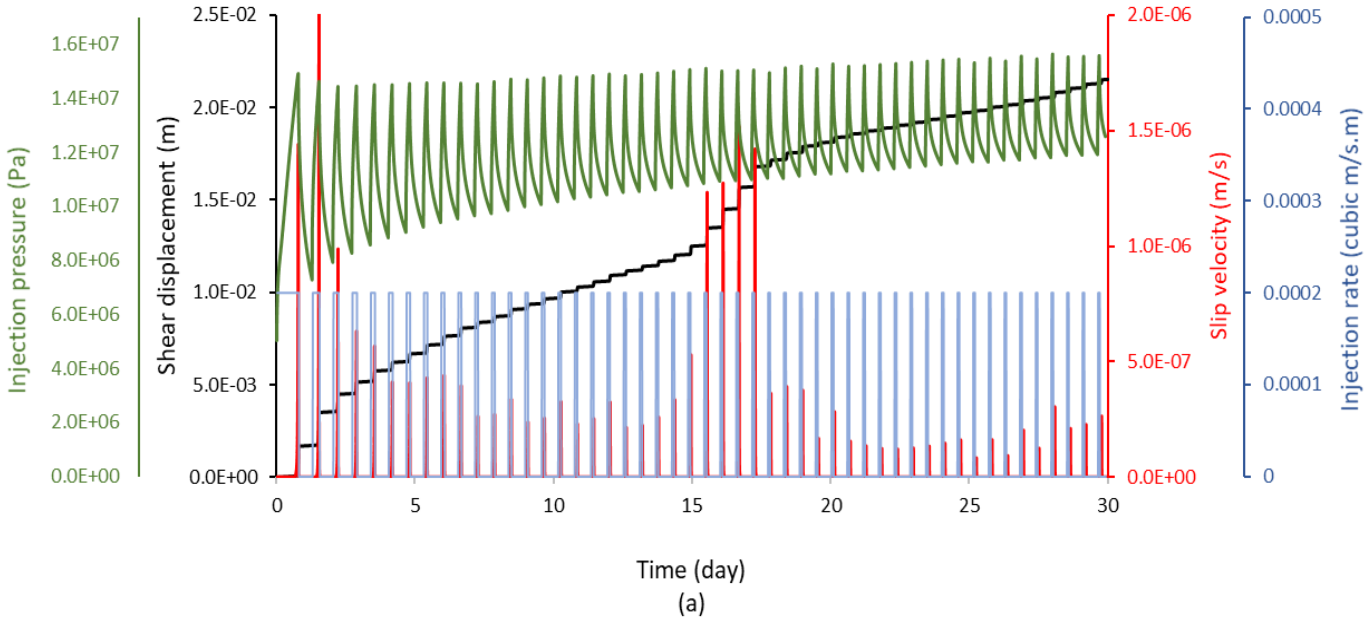
Injection pressure (Pa)
1.6E+07
1.4E+07
1.2E+07
1.0E+07
8.0E+06
6.0E+06
4.0E+06
2.0E+06
0.0E+00
Shear displacement (m)
2.5E-02
2.0E-02
1.5E-02
1.0E-02
5.0E-03
0.0E+00
Slip velocity (m/s)
2.0E-06
1.5E-06
1.0E-06
5.0E-07
0.0E+00
Injection rate (cubic m/s.m)
0.0005
0.0004
0.0003
0.0002
0.0001
0
0
5
10
15
20
25
30
Time (day)

(a)

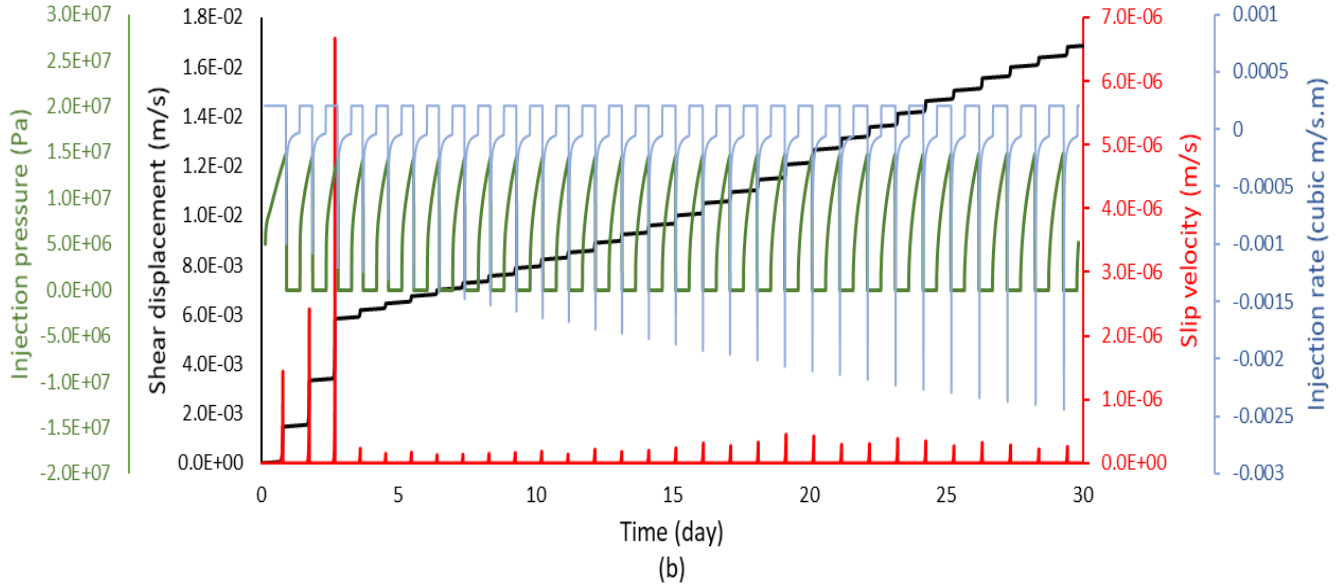
Injection pressure (Pa)
3.0E+07
2.5E+07
2.0E+07
1.5E+07
1.0E+07
5.0E+06
0.0E+00
-5.0E+06
-1.0E+07
-1.5E+07
-2.0E+07
Shear displacement (m/s)
1.8E-02
1.6E-02
1.4E-02
1.2E-02
1.0E-02
8.0E-03
6.0E-03
4.0E-03
2.0E-03
0.0E+00
Slip velocity (m/s)
7.0E-06
6.0E-06
5.0E-06
4.0E-06
3.0E-06
2.0E-06
1.0E-06
0.0E+00
Injection rate (cubic m/s.m)
0.001
0.0005
0
-0.0005
-0.001
-0.0015
-0.002
-0.0025
-0.003
0
5
10
15
20
25
30
Time (day)

(b)

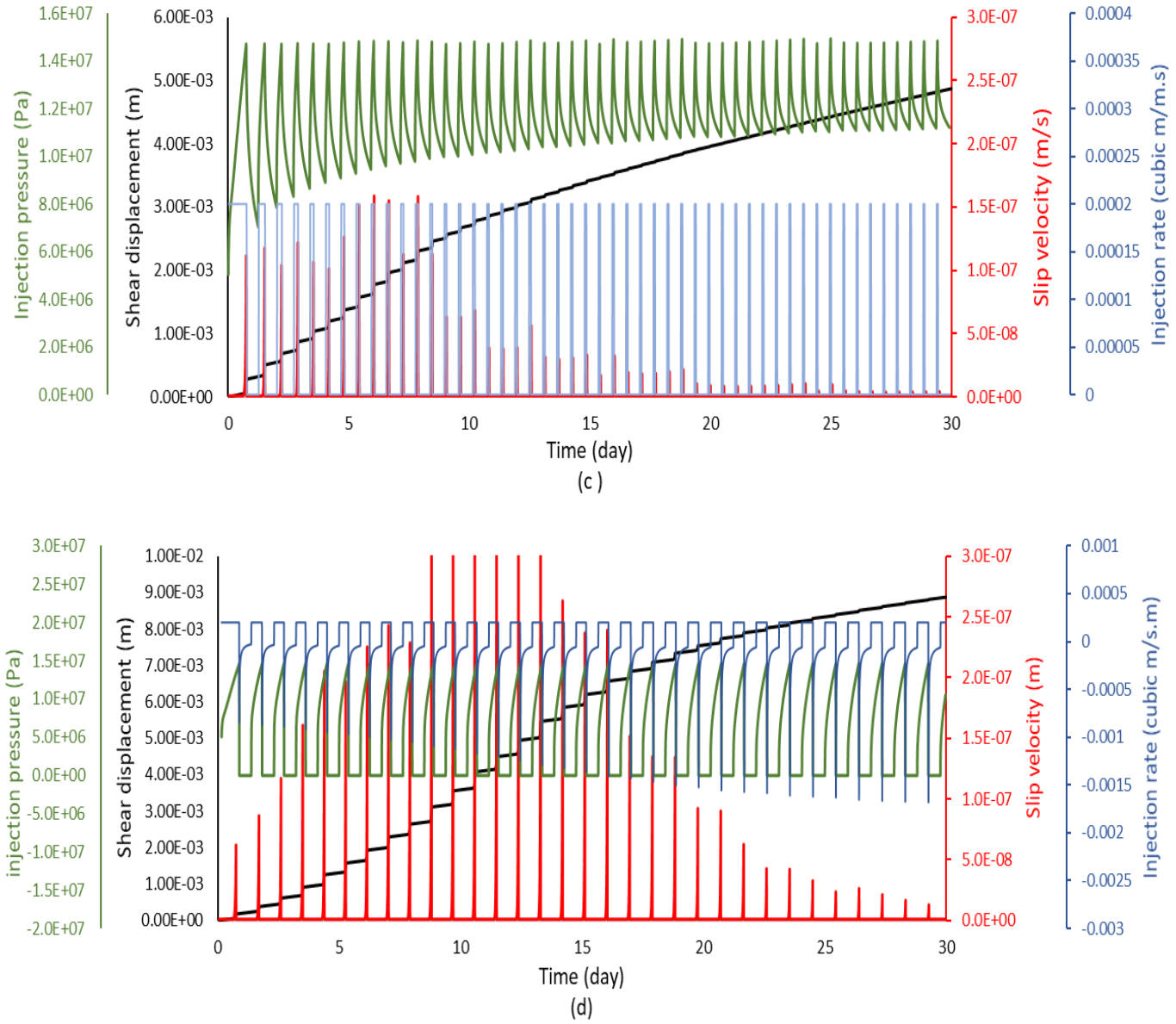

Fig. 17. Evaluation of shear displacement, slip rate, injection rate, and injection pressure for point P5 in the (a) cyclic injection based on TLS-without backflow, (b) cyclic injection based on TLS-with backflow, (c) cyclic injection based on VC-without backflow, and (d) cyclic injection based on VC-with backflow

This suggests that the TLS-based cyclic injection positively contributes to enhancing the conductivity of faults or natural fractures in low permeable reservoirs. This, in turn, would lead to a higher increase in the heat extraction efficiency of geothermal systems, where the natural fractures and faults play an important role in hydraulically connecting the extraction and injection wells. It is worth noting that the seismic risk associated with this type of cyclic injection is higher than other ones. According to the performed simulations, if the critical moment magnitude is not properly determined, cessation of fluid injection may not prevent the transition of some of aseismic slips to fully seismic events. The second-most efficient cyclic injection in terms of permeability enhancement is TLS with backflow. Applying this injection scheme brings about 8.83×10^{-4} m (8.83 times) increase in the fracture aperture. Despite causing a smaller increase in the aperture compared to the case of TLS-without backflow, the risk of earthquake nucleation during the post-injection stage is significantly reduced in this type of injection scheme. This is because fluid extraction constrains the fracture slip to only occur in the injection stage of each cycle and prevents additional slip in the post-injection stage.

VC with backflow is ranked third with inducing 4.65×10^{-4} m normal displacement to the fault initial width. In this injection scheme, the rate of increase in the fracture aperture gradually dwindles over time, indicating that this type of cyclic injection only contributes to permeability enhancement at early stages. In VC without backflow, the average fault aperture increases by 2.55×10^{-4} m (2.55 times enhancement) after 30 days of continuous cyclic injection, indicating this scheme as the least efficient injection style in terms of permeability enhancement. Hence, if permeability enhancement is prioritized, VC without backflow cannot serve as an efficient approach for the irreversible increase of fault aperture for a prolonged cyclic injection. However, it is a much safer injection style, as the yielded moment magnitude of each cycle is lower than the other three injection schemes (Fig. 19). These results indicate that cyclic injection based on VC generally does not promote the aseismic slip as much as those based on TLS. Nevertheless, fluid extraction (backflow) increases the efficiency of the VC-based injection schemes by encouraging fracture slip, while the opposite holds for cyclic injections based on TLS.

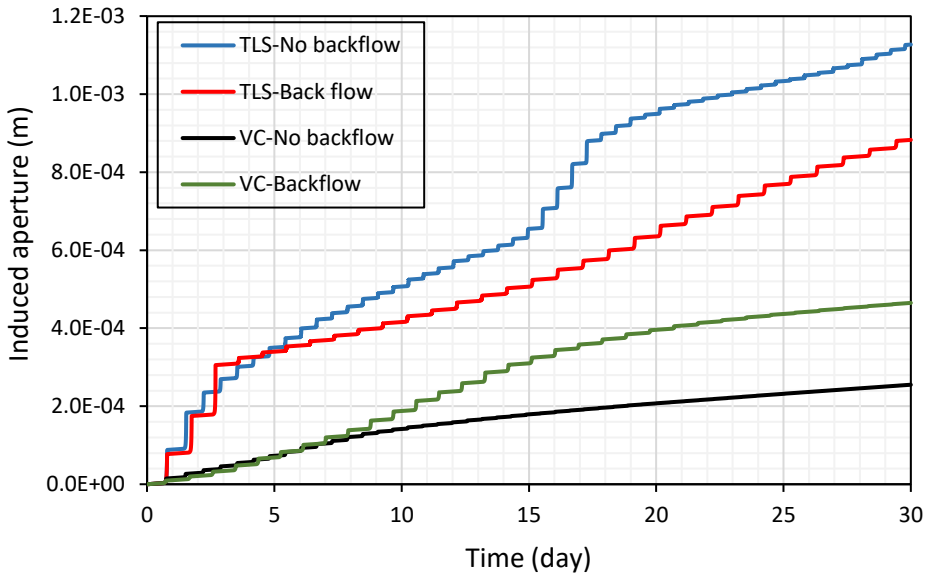

Fig. 18. Aperture increase as the function of time in different injection schemes

Fig. 19 shows the seismic moment and moment magnitude values in each cycle for the proposed cyclic injections. First of all, it is noticeable that fluid extraction during the post-injection stage reduces the total number of cycles for a specified time, which is also more significant in the case of the VC-based cyclic injection. Moment magnitude analysis corresponding to each cyclic injection can provide a better insight into which injection scheme poses a higher risk of earthquake nucleation. For TLS-without backflow, results show that some cycles lead to moment magnitudes higher than the critical moment magnitude of -0.1.

This is partly due to consideration of constant time-stepping in the thermo-poroelastic boundary element method. If the moment magnitude reaches its critical value within a particular time step, injection would not be terminated until reaching the end of that time step. This means that injection continues for a while after criteria satisfaction, leading to higher moment magnitudes than the critical value. The other reason behind this result corresponds to the slip tendency of fault after injection termination. The fault continues to slip to a limited extend for a very short time after stopping the injection, which causes moment magnitude to slightly exceed the prescribed critical value. It is worth noting that if termination of injection occurs with a slightly more delay after exceeding the critical moment magnitude, a limited fault slip during the post-injection stage may turn into an earthquake. Moment magnitudes associated with TLS-with backflow (Fig. 19) indicate that fluid extraction significantly prevents the occurrence of fast-

accelerated fracture slip during the post-injection stage. This, in turn, brings about lower moment magnitudes in each cycle and reduces the risk of earthquake nucleation during the post-injection stage. Regarding the VC-based injection schemes, the yielded moment magnitudes in all cycles remain below -0.2. This suggests that performing the cyclic injection, at which the criteria for the stop of injection is based on the fracture failure pressure, does not generally pose any seismic risk during the injection and post-injection stages.

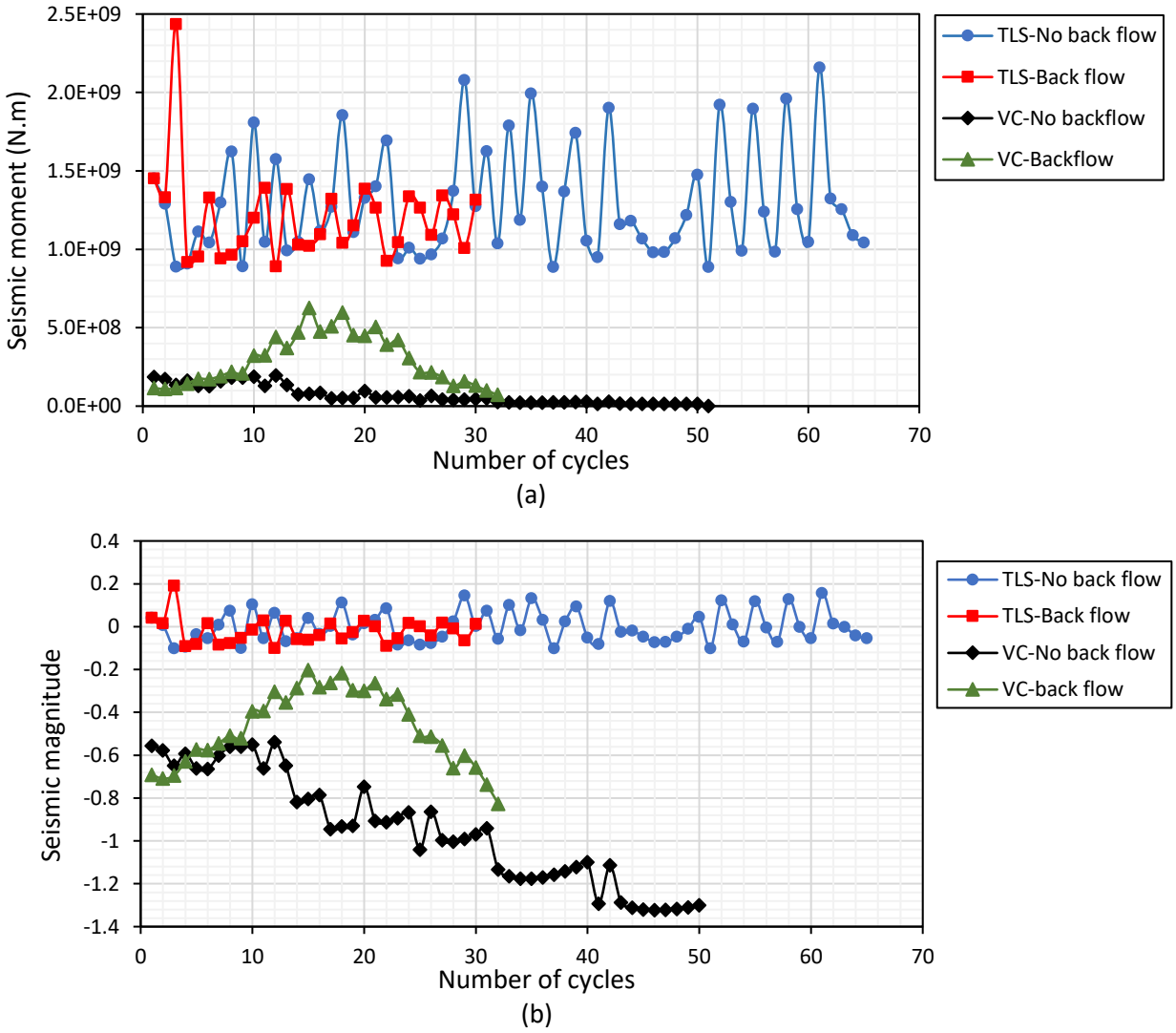

Fig. 19. (a) Seismic moment and (b) moment magnitude as functions of cycle number in the different cyclic injection schemes

5.3 Effect of temperature on dynamic instability

A comparison of isothermal and non-isothermal injection on dynamic instability is shown in Table 2. For isothermal and non-isothermal cases, the injection temperatures are set to be 420 and 300 K, respectively. Other parameters corresponding to fluid and rock properties (Table 1) are the same for both cases. The overall data comparison in Table 2 shows that the temperature difference between injected fluid and rock matrix has no significant effect on fault frictional behavior. However, non-isothermal injection slightly accelerates the occurrence of seismic events as effective normal stress decreases more due to induced thermal stresses. In addition, except for the first event, non-isothermal injection is associated with slightly higher seismic moments and moment magnitudes for the rest of the seismic events, indicating that increasing the injection temperature can potentially reduce the seismic magnitude in cases where the temperature effect would be significant. The average slip yielded by non-isothermal simulations is 0.157 m for the first seismic event, slightly lower than isothermal case (0.159 m). For the rest of the four events, non-isothermal injection leads to a higher seismic slip in comparison with isothermal injection. The same trends are also seen for the shear stress drop measured for each seismic event.

Table 2. Comparison of isothermal and non-isothermal injection on dynamic instability

Event Time (Day)		**Seismic Moment (N.m)**		**Moment Magnitude**		**Average Slip (m)**		**Stress drop (Pa)**	
Isothermal	Non-isothermal	Isothermal	Non-isothermal	Isothermal	Non-isothermal	Isothermal	Non-isothermal	Isothermal	Non-isothermal
10.27	10.00	1.904E+12	1.88544E+12	2.120	2.117	0.159	0.157	3163165	3145202
25.02	24.45	1.258E+12	1.2806E+12	2.000	2.005	0.105	0.107	2134196	2190018
41.03	40.18	8.115E+11	8.36494E+11	1.873	1.882	0.068	0.070	1373035	1438125
55.50	54.48	5.036E+11	5.34491E+11	1.735	1.752	0.042	0.045	861110	931496
67.27	66.22	2.712E+11	3.16045E+11	1.556	1.600	0.023	0.026	483636	567072

6. Conclusion

In this study, a two-dimensional fully coupled THM boundary element method is introduced. The model is used to investigate the fluid-injection-induced fault reactivation behavior and assess the efficiency of cyclic injection for enhancing the initial fault conductivity and reducing the seismicity-related risks. The model deploys rate-and-state friction law as the basis for the frictional contact algorithm, coupled with a thermo-poroelastic numerical solution algorithm. The elastic DD method as a complementary numerical approach is also used to implement the adaptive time stepping, so as to reach a good numerical resolution during the dynamic rupture. All Phases of stick-slip cycles are simulated to characterize the fault response to non-isothermal injection in terms of shear stress, slip rate, and aseismic and seismic slips. The modeling results show that nucleation of dynamic instability is associated with rupture propagation which accelerates along the fault. Acceleration of dynamic rupture causes a higher slip rate, peak strength, and static stress drop at the points located far from the injection area. However, it was observed that a prolonged injection eventually leads to an overall smaller peak slip rate, slip increment, and average stress drop. This, in turn, affects the released seismic energy during the full seismic events. We found that the seismic magnitude follows a decreasing trend with increasing the total injected fluid volume if the fluid is injected directly at the center of a single rate-and-state governed fault. This negative correlation is due to reduction in the absolute difference between the effective normal stress and static shear stress after a particular seismic event, which leads to lower slip rates and eventually less energy release in the subsequent event. After 67.27 days of continuous injection, the quasi-static deformation completely dominates the fault frictional behavior, and a total accumulated slip occurs as a stable and continuous slip with slip velocities below the seismic range.

The numerical experiments designed in this study also provide complementary insights into the potential of different injection styles in seismic risk mitigation and fracture permeability enhancement. Simulations showed that the proposed cyclic injection styles can effectively restrict the maximum peak slip rate and, therefore, prevent the nucleation of damaging earthquakes by promoting aseismic slip. We found that cyclic water injection, regardless of the style, cannot completely guarantee the aseismic fracture slip, but the VC-based fluid injection

yields a higher potential for mitigating the injection-induced seismic risk in comparison with those based on TLS. It is worth noting that fluid extraction during the post-injection stage positively contributes to seismic risk mitigation by restricting the fast and unstable fracture slips. Regarding permeability enhancement, the TLS-based injection schemes show higher efficiencies in improving the fracture permeability through the dilation effect. Results showed that it is possible to irreversibly increase the initial fault aperture by approximately ten times through applying a TLS-based fluid injection protocol.

Numerical modeling in a quasi-dynamic sense leads to lower slip increment and slip rate per each event in comparison with fully dynamic approach. Although reducing the radiation damping term in the quasi-dynamic technique rescales the resulting solutions, it fails to qualitatively change the results, especially for long-term slip patterns. This approach also fails to reproduce a supersheer burst when distribution of the normal stress is not uniform along the fault. Hence, implementing a thermo-poroelastic fully dynamic modeling would be an effective approach to capture a more realistic frictional behavior.

References

Almakari, M., Dublanchet, P., Chauris, H., & Pellet, F. (2019). Effect of the injection scenario on the rate and magnitude content of injection-induced seismicity: Case of a heterogeneous fault. *Journal of Geophysical Research: Solid Earth*, *124*(8), 8426-8448.

Andrés, S., Santillán, D., Mosquera, J. C., & Cueto-Felgueroso, L. (2019). Delayed weakening and reactivation of rate-and-state faults driven by pressure changes due to fluid injection. *Journal of Geophysical Research: Solid Earth*, *124*(11), 11917-11937.

Bandis, S., Lumsden, A., & Barton, N. (1983). Fundamentals of rock joint deformation. International Journal of Rock Mechanics and Mining Sciences & Geomechanics Abstracts,

Barton, N., Bandis, S., & Bakhtar, K. (1985). Strength, deformation and conductivity coupling of rock joints. International journal of rock mechanics and mining sciences & geomechanics abstracts,

Baumberger, T., & Caroli, C. (2006). Solid friction from stick–slip down to pinning and aging. *Advances in Physics*, *55*(3-4), 279-348.

Ben-Zion, Y., & Rice, J. R. (1997). Dynamic simulations of slip on a smooth fault in an elastic solid. *Journal of Geophysical Research: Solid Earth*, *102*(B8), 17771-17784.

Bhattacharya, P., Rubin, A. M., Bayart, E., Savage, H. M., & Marone, C. (2015). Critical evaluation of state evolution laws in rate and state friction: Fitting large velocity steps in simulated fault gouge with time-, slip-, and stress-dependent constitutive laws. *Journal of Geophysical Research: Solid Earth*, *120*(9), 6365-6385.

Bhattacharya, P., Rubin, A. M., & Beeler, N. M. (2017). Does fault strengthening in laboratory rock friction experiments really depend primarily upon time and not slip? *Journal of Geophysical Research: Solid Earth*, *122*(8), 6389-6430.

Brace, W., & Byerlee, J. (1966). Stick-slip as a mechanism for earthquakes. *Science*, *153*(3739), 990-992.

Brodsky, E. E., & Lajoie, L. J. (2013). Anthropogenic seismicity rates and operational parameters at the Salton Sea Geothermal Field. *Science*, *341*(6145), 543-546.

Brooks, A. N., & Hughes, T. J. (1982). Streamline upwind/Petrov-Galerkin formulations for convection dominated flows with particular emphasis on the incompressible Navier-Stokes equations. *Computer methods in applied mechanics and engineering*, *32*(1-3), 199-259.

Cesca, S., Grigoli, F., Heimann, S., González, A., Buforn, E., Maghsoudi, S., Blanch, E., & Dahm, T. (2014). The 2013 September–October seismic sequence offshore Spain: a case of seismicity triggered by gas injection? *Geophysical Journal International*, *198*(2), 941-953.

Chang, K. W., & Segall, P. (2016a). Injection-induced seismicity on basement faults including poroelastic stressing. *Journal of Geophysical Research: Solid Earth*, *121*(4), 2708-2726.

Chang, K. W., & Segall, P. (2016b). Seismicity on basement faults induced by simultaneous fluid injection–extraction. *pure and applied geophysics*, *173*(8), 2621-2636.

Cheng, A.-D., & Detournay, E. (1998). On singular integral equations and fundamental solutions of poroelasticity. *International journal of solids and structures*, *35*(34-35), 4521-4555.

Cheng, A. D., Ghassemi, A., & Detournay, E. (2001). Integral equation solution of heat extraction from a fracture in hot dry rock. *International Journal for Numerical and Analytical Methods in Geomechanics*, *25*(13), 1327-1338.

Cheng, A. H.-D. (2016). *Poroelasticity* (Vol. 877). Springer.

Cousse, J., Trutnevyte, E., & Hahnel, U. J. (2021). Tell me how you feel about geothermal energy: Affect as a revealing factor of the role of seismic risk on public acceptance. *Energy Policy*, *158*, 112547.

Crouch, S. L., Starfield, A. M., & Rizzo, F. (1983). Boundary element methods in solid mechanics.

Cueto-Felgueroso, L., Santillán, D., & Mosquera, J. C. (2017). Stick-slip dynamics of flow-induced seismicity on rate and state faults. *Geophysical Research Letters*, *44*(9), 4098-4106.

Cueto-Felgueroso, L., Vila, C., Santillán, D., & Mosquera, J. C. (2018). Numerical modeling of injection-induced earthquakes using laboratory-derived friction laws. *Water Resources Research*, *54*(12), 9833-9859.

Curran, J., & Carvalho, J. L. (1987). A displacement discontinuity model for fluid-saturated porous media. 6th ISRM Congress,

Day, S. M., Dalguer, L. A., Lapusta, N., & Liu, Y. (2005). Comparison of finite difference and boundary integral solutions to three-dimensional spontaneous rupture. *Journal of Geophysical Research: Solid Earth*, *110*(B12).

De Simone, S., Carrera, J., & Vilarrasa, V. (2017). Superposition approach to understand triggering mechanisms of post-injection induced seismicity. *Geothermics*, *70*, 85-97.

Deng, K., Liu, Y., & Harrington, R. M. (2016). Poroelastic stress triggering of the December 2013 Crooked Lake, Alberta, induced seismicity sequence. *Geophysical Research Letters*, *43*(16), 8482-8491.

Diersch, H.-J. G. (2013). *FEFLOW: finite element modeling of flow, mass and heat transport in porous and fractured media*. Springer Science & Business Media.

Dieterich, J. H. (1978). Time-dependent friction and the mechanics of stick-slip. In *Rock friction and earthquake prediction* (pp. 790-806). Springer.

Dieterich, J. H. (1979). Modeling of rock friction: 1. Experimental results and constitutive equations. *Journal of Geophysical Research: Solid Earth*, *84*(B5), 2161-2168.

Dou, Z., Gao, T., Zhao, Z., Li, J., Yang, Q., & Shang, D. (2020). The role of water lubrication in critical state fault slip. *Engineering Geology*, *271*, 105606.

Ebrahimi, M., Ameri, M. J., Vaghasloo, Y. A., & Sabah, M. (2021). Fully coupled thermo-hydro-mechanical approach to model fracture response to injection process in enhanced geothermal systems using

displacement discontinuity and finite element method. *Journal of Petroleum Science and Engineering*, 109240.

Galis, M., Ampuero, J. P., Mai, P. M., & Cappa, F. (2017). Induced seismicity provides insight into why earthquake ruptures stop. *Science advances*, *3*(12), eaap7528.

Gan, Q., & Lei, Q. (2020). Induced fault reactivation by thermal perturbation in enhanced geothermal systems. *Geothermics*, *86*, 101814.

Guglielmi, Y., Cappa, F., Avouac, J.-P., Henry, P., & Elsworth, D. (2015). Seismicity triggered by fluid injection–induced aseismic slip. *Science*, *348*(6240), 1224-1226.

Haddad, M., & Eichhubl, P. (2020). Poroelastic models for fault reactivation in response to concurrent injection and production in stacked reservoirs. *Geomechanics for Energy and the Environment*, *24*, 100181.

Hofmann, H., Zimmermann, G., Huenges, E., Regenspurg, S., Aldaz, S., Milkereit, C., Heimann, S., Dahm, T., Zang, A., & Grigoli, F. (2021). Soft stimulation treatment of geothermal well RV-43 to meet the growing heat demand of Reykjavik. *Geothermics*, *96*, 102146.

Hui, G., Chen, S., Chen, Z., & Gu, F. (2021). An integrated approach to characterize hydraulic fracturing-induced seismicity in shale reservoirs. *Journal of Petroleum Science and Engineering*, *196*, 107624.

Hui, G., Chen, S., Gu, F., Wang, H., Zhang, L., & Yu, X. (2021). Influence of hydrological communication between basement-rooted faults and hydraulic fractures on induced seismicity: A case study. *Journal of Petroleum Science and Engineering*, 109040.

Jeanne, P., Rutqvist, J., & Dobson, P. F. (2017). Influence of injection-induced cooling on deviatoric stress and shear reactivation of preexisting fractures in Enhanced Geothermal Systems. *Geothermics*, *70*, 367-375.

Ji, Y., Yoon, J. S., Zang, A., & Wu, W. (2021). Mitigation of injection-induced seismicity on undrained faults in granite using cyclic fluid injection: A laboratory study. *International Journal of Rock Mechanics and Mining Sciences*, *146*, 104881.

Ji, Y., Zhuang, L., Wu, W., Hofmann, H., Zang, A., & Zimmermann, G. (2021). Cyclic Water Injection Potentially Mitigates Seismic Risks by Promoting Slow and Stable Slip of a Natural Fracture in Granite. *Rock Mechanics and Rock Engineering*, 1-17.

Kato, N., & Tullis, T. E. (2001). A composite rate-and state-dependent law for rock friction. *Geophysical Research Letters*, *28*(6), 1103-1106.

Kettlety, T., Verdon, J. P., Werner, M. J., & Kendall, J. (2020). Stress transfer from opening hydraulic fractures controls the distribution of induced seismicity. *Journal of Geophysical Research: Solid Earth*, *125*(1), e2019JB018794.

Khademian, Z., Nakagawa, M., & Ozbay, U. (2018). Modeling injection-induced seismicity through calculation of radiated seismic energy. *Journal of Natural Gas Science and Engineering*, *52*, 582-590.

Kim, S., & Hosseini, S. A. (2015). Hydro-thermo-mechanical analysis during injection of cold fluid into a geologic formation. *International Journal of Rock Mechanics and Mining Sciences*, *77*, 220-236.

Knoblauch, T. A., Stauffacher, M., & Trutnevyte, E. (2018). Communicating low-probability high-consequence risk, uncertainty and expert confidence: Induced seismicity of deep geothermal energy and shale gas. *Risk Analysis*, *38*(4), 694-709.

Kroll, K. A., Richards-Dinger, K. B., & Dieterich, J. H. (2017). Sensitivity of induced seismic sequences to rate-and-state frictional processes. *Journal of Geophysical Research: Solid Earth*, *122*(12), 10,207-210,219.

Lapusta, N., & Liu, Y. (2009). Three-dimensional boundary integral modeling of spontaneous earthquake sequences and aseismic slip. *Journal of Geophysical Research: Solid Earth*, *114*(B9).

Lapusta, N., Rice, J. R., Ben-Zion, Y., & Zheng, G. (2000). Elastodynamic analysis for slow tectonic loading with spontaneous rupture episodes on faults with rate-and state-dependent friction. *Journal of Geophysical Research: Solid Earth*, *105*(B10), 23765-23789.

Linker, M., & Dieterich, J. H. (1992). Effects of variable normal stress on rock friction: Observations and constitutive equations. *Journal of Geophysical Research: Solid Earth*, *97*(B4), 4923-4940.

Liu, Y., & Rice, J. R. (2005). Aseismic slip transients emerge spontaneously in three-dimensional rate and state modeling of subduction earthquake sequences. *Journal of Geophysical Research: Solid Earth*, *110*(B8).

Marone, C. (1998). Laboratory-derived friction laws and their application to seismic faulting. *Annual Review of Earth and Planetary Sciences*, *26*(1), 643-696.

Maxwell, J. C. (1864). L. on the calculation of the equilibrium and stiffness of frames. *The London, Edinburgh, and Dublin Philosophical Magazine and Journal of Science*, *27*(182), 294-299.

McGarr, A., & Barbour, A. J. (2018). Injection-induced moment release can also be aseismic. *Geophysical Research Letters*, *45*(11), 5344-5351.

Mitsui, Y., & Hirahara, K. (2009). Coseismic thermal pressurization can notably prolong earthquake recurrence intervals on weak rate and state friction faults: Numerical experiments using different constitutive equations. *Journal of Geophysical Research: Solid Earth*, *114*(B9).

Nagata, K., Nakatani, M., & Yoshida, S. (2012). A revised rate-and state-dependent friction law obtained by constraining constitutive and evolution laws separately with laboratory data. *Journal of Geophysical Research: Solid Earth*, *117*(B2).

Noël, C., Passelègue, F. X., Giorgetti, C., & Violay, M. (2019). Fault reactivation during fluid pressure oscillations: Transition from stable to unstable slip. *Journal of Geophysical Research: Solid Earth*, *124*(11), 10940-10953.

Pampillon, P., Santillán, D., Mosquera, J. C., & Cueto-Felgueroso, L. (2018). Dynamic and quasi-dynamic modeling of injection-induced earthquakes in poroelastic media. *Journal of Geophysical Research: Solid Earth*, *123*(7), 5730-5759.

Park, J.-W., Guglielmi, Y., Graupner, B., Rutqvist, J., Kim, T., Park, E.-S., & Lee, C. (2020). Modeling of fluid injection-induced fault reactivation using coupled fluid flow and mechanical interface model. *International Journal of Rock Mechanics and Mining Sciences*, *132*, 104373.

Putelat, T., Dawes, J. H., & Willis, J. R. (2011). On the microphysical foundations of rate-and-state friction. *Journal of the Mechanics and Physics of Solids*, *59*(5), 1062-1075.

Rathnaweera, T. D., Wu, W., Ji, Y., & Gamage, R. P. (2020). Understanding injection-induced seismicity in enhanced geothermal systems: From the coupled thermo-hydro-mechanical-chemical process to anthropogenic earthquake prediction. *Earth-Science Reviews*, *205*, 103182.

Rice, J. R. (1983). Constitutive relations for fault slip and earthquake instabilities. In *Instabilities in continuous media* (pp. 443-475). Springer.

Rice, J. R. (1993). Spatio-temporal complexity of slip on a fault. *Journal of Geophysical Research: Solid Earth*, *98*(B6), 9885-9907.

Rice, J. R., & Ruina, A. L. (1983). Stability of steady frictional slipping.

Rinaldi, A. P., & Nespoli, M. (2017). TOUGH2-seed: A coupled fluid flow and mechanical-stochastic approach to model injection-induced seismicity. *Computers & Geosciences*, *108*, 86-97.

Rubin, A. M., & Ampuero, J. P. (2005). Earthquake nucleation on (aging) rate and state faults. *Journal of Geophysical Research: Solid Earth*, *110*(B11).

Ruina, A. (1983). Slip instability and state variable friction laws. *Journal of Geophysical Research: Solid Earth*, *88*(B12), 10359-10370.

Safari, R., & Ghassemi, A. (2016). Three-dimensional poroelastic modeling of injection induced permeability enhancement and microseismicity. *International Journal of Rock Mechanics and Mining Sciences*, *84*, 47-58.

Scholz, C. H. (1998). Earthquakes and friction laws. *Nature*, *391*(6662), 37-42.

Segall, P., & Lu, S. (2015). Injection-induced seismicity: Poroelastic and earthquake nucleation effects. *Journal of Geophysical Research: Solid Earth*, *120*(7), 5082-5103.

Shirzaei, M., Ellsworth, W. L., Tiampo, K. F., González, P. J., & Manga, M. (2016). Surface uplift and time-dependent seismic hazard due to fluid injection in eastern Texas. *Science*, *353*(6306), 1416-1419.

Shreedharan, S., Rivière, J., Bhattacharya, P., & Marone, C. (2019). Frictional state evolution during normal stress perturbations probed with ultrasonic waves. *Journal of Geophysical Research: Solid Earth*, *124*(6), 5469-5491.

Sneddon, I. N. (1946). The distribution of stress in the neighbourhood of a crack in an elastic solid. *Proceedings of the Royal Society of London. Series A. Mathematical and Physical Sciences*, *187*(1009), 229-260.

Taghipour, M., Ghafoori, M., Lashkaripour, G. R., Moghaddas, N. H., & Molaghab, A. (2021). A Geomechanical Evaluation of Fault Reactivation Using Analytical Methods and Numerical Simulation. *Rock Mechanics and Rock Engineering*, *54*(2), 695-719.

Tao, Q. (2010). *Numerical modeling of fracture permeability change in naturally fractured reservoirs using a fully coupled displacement discontinuity method*. Texas A&M University.

Thompson, T. B., & Meade, B. J. (2019). Boundary element methods for earthquake modeling with realistic 3D geometries.

Vadacca, L., Rossi, D., Scotti, A., & Buttinelli, M. (2021). Slip tendency analysis, fault reactivation potential and induced seismicity in the Val d'Agri oilfield (Italy). *Journal of Geophysical Research: Solid Earth*, *126*(1), 2019JB019185.

Van den Ende, M., Chen, J., Ampuero, J.-P., & Niemeijer, A. (2018). A comparison between rate-and-state friction and microphysical models, based on numerical simulations of fault slip. *Tectonophysics*, *733*, 273-295.

Van der Elst, N. J., Page, M. T., Weiser, D. A., Goebel, T. H., & Hosseini, S. M. (2016). Induced earthquake magnitudes are as large as (statistically) expected. *Journal of Geophysical Research: Solid Earth*, *121*(6), 4575-4590.

Verde, A., & Ghassemi, A. (2016). Large-scale poroelastic fractured reservoirs modeling using the fast multipole displacement discontinuity method. *International Journal for Numerical and Analytical Methods in Geomechanics*, *40*(6), 865-886.

Wang, L., Kwiatek, G., Rybacki, E., Bonnelye, A., Bohnhoff, M., & Dresen, G. (2020). Laboratory study on fluid-induced fault slip behavior: The role of fluid pressurization rate. *Geophysical Research Letters*, *47*(6), e2019GL086627.

Wassing, B., Gan, Q., Candela, T., & Fokker, P. (2021). Effects of fault transmissivity on the potential of fault reactivation and induced seismicity: Implications for understanding induced seismicity at Pohang EGS. *Geothermics*, *91*, 101976.

Witherspoon, P. A., Wang, J. S., Iwai, K., & Gale, J. E. (1980). Validity of cubic law for fluid flow in a deformable rock fracture. *Water resources research*, *16*(6), 1016-1024.

Wriggers, P., & Laursen, T. A. (2006). *Computational contact mechanics* (Vol. 2). Springer.

Wu, H., Vilarrasa, V., De Simone, S., Saaltink, M., & Parisio, F. (2021). Analytical solution to assess the induced seismicity potential of faults in pressurized and depleted reservoirs. *Journal of Geophysical Research: Solid Earth*, *126*(1), e2020JB020436.

XinXin, Y., ChangSheng, J., HongYu, Z., YanBao, Z., Cong, J., GuiJuan, L., AiYu, Z., & FengLing, Y. (2021). Review of induced seismicity and disaster risk control in dry hot rock resource development worldwide. *Chinese Journal of Geophysics*, *64*(11), 3817-3836.

Ye, Z., & Ghassemi, A. (2018). Injection-induced shear slip and permeability enhancement in granite fractures. *Journal of Geophysical Research: Solid Earth*, *123*(10), 9009-9032.

Yew, C. (1997). Mechanics of Hydraulic Fracturing, Houston, TX; Gulf Pub. In: Co.

Yin, Z., Huang, H., Zhang, F., Zhang, L., & Maxwell, S. (2020). Three-dimensional distinct element modeling of fault reactivation and induced seismicity due to hydraulic fracturing injection and backflow. *Journal of Rock Mechanics and Geotechnical Engineering*, *12*(4), 752-767.

Zang, A., Zimmermann, G., Hofmann, H., Stephansson, O., Min, K.-B., & Kim, K. Y. (2019). How to reduce fluid-injection-induced seismicity. *Rock Mechanics and Rock Engineering*, *52*(2), 475-493.

Zhang, Q. (2004). A boundary element method for thermo-poroelasticity with applications in rock mechanics.

Zimmerman, R. W., & Bodvarsson, G. S. (1996). Hydraulic conductivity of rock fractures. *Transport in porous media*, *23*(1), 1-30.

Ziv, A., & Cochard, A. (2006). Quasi-dynamic modeling of seismicity on a fault with depth-variable rate- and state-dependent friction. *Journal of Geophysical Research: Solid Earth*, *111*(B8).

Zoback, M. D., & Gorelick, S. M. (2012). Earthquake triggering and large-scale geologic storage of carbon dioxide. *Proceedings of the National Academy of Sciences*, *109*(26), 10164-10168.